Direct numerical simulation of flow over dissimilar, randomly distributed roughness elements: A systematic study on the effect of surface morphology on turbulence

Pourya Forooghi,[1,*] Alexander Stroh,[1] Philipp Schlatter,[2] and Bettina Frohnapfel[1]
[1]*Institute of Fluid Mechanics, Karlsruhe Institute of Technology, 76131 Karlsruhe, Germany*
[2]*Linné FLOW Centre, KTH Royal Institute of Technology, 114 28 Stockholm, Sweden*

(Received 24 October 2017; published 25 April 2018)

Direct numerical simulations are used to investigate turbulent flow in rough channels, in which topographical parameters of the rough wall are systematically varied at a fixed friction Reynolds number of 500, based on a mean channel half-height h and friction velocity. The utilized roughness generation approach allows independent variation of moments of the surface height probability distribution function [thus root-mean-square (rms) surface height, skewness, and kurtosis], surface mean slope, and standard deviation of the roughness peak sizes. Particular attention is paid to the effect of the parameter Δ defined as the normalized height difference between the highest and lowest roughness peaks. This parameter is used to understand the trends of the investigated flow variables with departure from the idealized case where all roughness elements have the same height ($\Delta = 0$). All calculations are done in the fully rough regime and for surfaces with high slope (effective slope equal to 0.6–0.9). The rms roughness height is fixed for all cases at $0.045h$ and the skewness and kurtosis of the surface height probability density function vary in the ranges -0.33 to 0.67 and 1.9 to 2.6, respectively. The goal of the paper is twofold: first, to investigate the possible effect of topographical parameters on the mean turbulent flow, Reynolds, and dispersive stresses particularly in the vicinity of the roughness crest, and second, to investigate the possibility of using the wall-normal turbulence intensity as a physical parameter for parametrization of the flow. Such a possibility, already suggested for regular roughness in the literature, is here extended to irregular roughness.

DOI: 10.1103/PhysRevFluids.3.044605

I. INTRODUCTION

The study of rough wall-bounded turbulence finds application in a wide range of problems, piping systems, gas turbines, marine vehicles, river flows, and atmospheric boundary layers over (urban or forest) canopies being typical examples [1]. In the past few decades, the fluid mechanics research in this field has been mainly focused on two issues: On the engineering side, there have been attempts to find a correlation between roughness geometrical properties such as surface mean slope [2], surface height distribution moments [3], and roughness density [4,5] and equivalent sand roughness or other skin-friction-related quantities; on the turbulence physics side, considerable effort has been devoted to understanding the inner-layer–outer-layer interactions and the validity of outer-layer similarity as stated by Townsend [6]. In this regard, Flack *et al.* [7], showed, by examining flow over sandpaper and woven wire mesh, that for a flat plate turbulent boundary layer well downstream of the tripping point, the effect of roughness on the first- and second-order statistics is only sensed up to five roughness heights, a distance referred to as the roughness sublayer thickness. Further details on the outer-layer

*forooghi@kit.edu

similarity can be found in the comprehensive review by Flack and Schultz [8] and recent boundary layer experimental results by Squire *et al.* [9], among others. Compared to the two above-mentioned research directions, relatively less attention has been paid to the effect of roughness morphology on the turbulence within the roughness sublayer, even though one can find a number of insightful papers in which a range of roughness geometries is examined. For instance, Leonardi *et al.* [10] used direct numerical simulation (DNS) to study channel flow with spanwise square bars attached on the wall and varied the spacing ratio of the bars in order to observe the transition from k- to d-type roughness. Schultz and Flack [11] used pyramids with different angles and heights to experimentally investigate the effect of surface slope on the scaling of roughness function (the downward shift in the logarithmic velocity profile due to roughness). Leonardi and Castro [12] (channel DNS) and Placidi and Ganapathisubramani [13] (boundary layer experiments) both used combinations of cubic elements mounted on a smooth wall in order to systematically investigate the effect of roughness density on the drag and turbulence field. The distance from the wall, beyond which there is no significant difference among Reynolds stress profiles of different surfaces, was reported to be $2k$ in the former and $2k$–$5k$ in the latter reference, k being the roughness element height. Both values agree with the previously mentioned estimation of viscous sublayer thickness [7] even though the ratios of roughness height to boundary layer thickness or channel height adopted by the recent authors are significantly smaller than that of Ref. [7]. Placidi and Ganapathisubramani [13] also found that the thickness of the roughness sublayer can be affected by roughness morphology. Recently, Chan *et al.* [14] numerically investigated the flow in pipes with three-dimensional (3D) sinusoidal roughness and systematically studied the effect of roughness height and wavelength (thus surface slope) to conclude that a combination of the two parameters can properly characterize the flow over a rough wall. A common simplification in all the above-mentioned works is the use of similar-size roughness elements (or waves) distributed in a regular way, which cannot be readily related to the industrial roughness often formed due to natural and random processes, thus being strongly irregular.

Since the landmark paper of Nikuradse [15], equivalent sand roughness height has been predominantly used in research and engineering as a means of characterization of rough walls. Despite its practicality, one needs to keep in mind that, except for the uniform sand-grain roughness tested in Nikuradse's experiments, this quantity is not a physical measure of the roughness, but rather an effective flow property. This serves as a motivation to look for alternative approaches with a more clear physical meaning to parametrize the roughness [16]. One such approach is using the velocity fluctuations instead of equivalent sand roughness. The idea stems originally from the channel DNS carried out by Orlandi *et al.* [17] in which nonzero fluctuating velocity components are imposed at the wall. It was observed by these authors that use of a nonzero wall-normal component results in structural changes in the flow similar to what is already observed in the flow over rough walls. This lent support to the idea that fluctuating velocities can be alternative quantities for parametrization of flow over rough walls. Orlandi and Leonardi further investigated this hypothesis by performing DNS in channels with 2D square bars and 3D roughness elements (cubes, cylinders, and wedges) of similar size and showed that the roughness function indeed correlates with root-mean-square wall-normal fluctuating velocity at the plane of the crests, i.e., $v^+_{\mathrm{rms}}|_{y_C}$ [18,19]. Here y_C denotes the wall-normal location of the plane of crests and the subscript rms indicates the root mean square of fluctuations averaged in wall-parallel directions and time. Orlandi and Leonardi [19] suggested a linear relation between the roughness function and $v^+_{\mathrm{rms}}|_{y_C}$ for fully rough flows

$$\Delta\tilde{U}^+_C = \frac{B v^+_{\mathrm{rms}}|_{y_C}}{\kappa}, \tag{1}$$

where B and κ are the logarithmic-law intercept and von Kármán constant, respectively, and $\Delta\tilde{U}^+_C$ denotes a variant of the roughness function defined by those authors. The exact definitions of $\Delta\tilde{U}^+_C$ and $v^+_{\mathrm{rms}}|_{y_C}$ will be discussed in Sec. IV C. This relation is of key importance since it implies that an expression for the mean velocity can be found in which the equivalent sand roughness is replaced by the wall-normal fluctuating velocity. Later on, Orlandi also described the laminar-turbulence transition threshold in a channel in terms of the same quantity, i.e., $v^+_{\mathrm{rms}}|_{yc}$ [20].

The correlation between roughness function and wall-normal turbulence fluctuation, i.e., Eq. (1), has been independently confirmed by DNS data of Lee *et al.* [21] for cubic roughness elements and Chan *et al.* [14] for 3D sinusoidal surfaces. Apart from the physical insight they provide, such results are of high practical significance as they may open up the opportunity to develop a new class of turbulence models for rough surfaces, which are based on prescription of turbulence fluctuations ($v^+_{\mathrm{rms}}|_{yc}$) on the boundary. It is reasonable to expect better predictions of turbulence structures in the roughness sublayer from such models since they are based on a quantity that directly reflects the physics of turbulence in the vicinity of the rough surface. Clearly, considerable effort is required to turn this physically justified idea into a working model. It is, however, important before such an effort is made to have a sufficient amount of data in support of the idea and, in particular, its central component, which is the existence of a correlation between roughness function and wall-normal turbulence fluctuation. The references mentioned above provide evidence of the validity of this hypothesis for their investigated type of geometries. Nevertheless, these investigated geometries all consist of similar-shape and regularly distributed roughness elements or sinusoidal waves, which is fairly far from generic. The lack of data on irregular roughness calls for further investigation.

A fundamental problem faced in the use of the above-mentioned hypothesis for the irregular roughness is the definition of the plane of the crests for such a roughness, as in this case, unlike in a regular roughness, the roughness peaks have different heights. In fact, there is no clear-cut definition of crest in an irregular roughness, hence one can try to find an effective plane of crests. Orlandi and Leonardi [19] suggested that the location of the highest peak can be used as the crest plane for an irregular roughness. Another possible choice may be the average height of all roughness peaks. The present work is a systematic investigation based on extensive data.

As already discussed, outer-layer similarity entails independence of turbulence statistics from the roughness geometry outside the roughness sublayer. It is however not the case in the immediate vicinity of roughness peaks, where surface parameters, i.e., statistical properties of the rough surface geometry, are expected to affect the turbulence. Therefore, any investigation of the flow inside the roughness sublayer should ideally account for the effect of roughness geometry. One group of surface parameters, which can be used to parametrize the texture of a rough surface, are those based on the probability density function (PDF) of surface height. It is shown that moments of this PDF (shortly surface moments), i.e., rms surface height, skewness, and kurtosis, can control the roughness function [3,8]. Surface slope is another parameter, which is widely believed to impact the rough-wall turbulence [11,22,23]. Another factor that can influence the problem is the nonuniformity of roughness peaks. It has been shown that equivalent sand roughness has a meaningful trend with the relative height difference between the tallest and the shortest peaks [24]; at fixed surface moments and mean slope, a roughness with uniform peaks has a higher friction factor than one with nonuniform peaks.

Direct numerical simulation is an effective tool in the evaluation of turbulence statistics inside the roughness sublayer, since it does not have the limitations of experimental measurements near or below the roughness crest. It has been argued by Orlandi and Leonardi [18] that only DNS can be used to exactly evaluate turbulence intensities at and below the crest level despite the disadvantage of limitation in Reynolds number. There has been a fairly large number of DNS studies on roughness in the past 15 years. However, as already pointed out, these studied cases have predominantly belonged to the category of regular roughness: roughness generated by regular distribution of similar-size elements, namely, cubes [12,18,19,21], cylinders [19], wedges [19,20], spheres [25,26], egg-carton shapes [27,28], and pyramids [29]. The 3D sinusoidal surfaces examined in Ref. [14] could also be classified in the same category. In contrast, a rather limited number of reports can be found in the literature on irregular surfaces. Cardillo *et al.* [30] carried out zero-pressure-gradient boundary layer DNS on a sandpaper surface roughness and observed the most noticeable difference between smooth and rough walls in the wall-normal and shear Reynolds stresses. Moreover, they observed, by performing proper orthogonal decomposition, an increase in the size of injection events in the first mode of the wall-normal component, which was attributed to the enhancement of mixing due to roughness. In one of the most comprehensive DNS reports on irregular roughness, Thakkar *et al.* [31] examined several industrially relevant surfaces in channels with two rough walls at relatively low Reynolds number ($\mathrm{Re}_\tau = 180$). They mainly focused on the scaling of the roughness function and clearly showed that surface morphology is a key parameter in the determination of flow properties. Busse *et al.* [32] performed DNS for one of the scanned surfaces used in Ref. [31]. They studied the effect of the resolution by which the surface is described on the resulting flow. Chau and Bhaganagar [34,35] performed DNS of flow over irregular ripples relevant in the coastal applications at $\mathrm{Re}_\tau = 180$. They systematically varied the mean wavelength of their highly anisotropic roughness geometry while keeping the height constant, thereby studying the effect of ripple spacing and surface slope on the velocity and vorticity statistics. Yuan and Piomelli [23] conducted highly resolved large-eddy simulation (LES) for five realistic roughness samples with a relatively low roughness slope. They mainly concentrated on the applicability of different correlation types for the calculation of equivalent sand roughness. They also compared the inner-scaled profiles of Reynolds stress inside the roughness sublayer and confirmed that the streamwise component is damped strongly in this region, leading to a more isotropic turbulence, an established characteristic of fully rough flow suggested by earlier authors, for example, in Ref. [33].

In the present paper we address irregular roughness, by using random distributions of dissimilar roughness elements for the generation of the surface samples. The roughness generation approach used in this research allows independent variation of several surface parameters and thereby enables a systematic investigation in a wide range of the parameter space. In this research we independently study three roughness parameters, namely, the skewness of the surface height PDF, the standard deviation of peak heights, and, to some extent, the mean surface slope. We believe that, on account of the sensitivity of the flow inside the roughness sublayer to the geometrical parameters, such a systematic investigation is necessary in order to avoid inadequate generalization of the results. The flow is simulated in a so-called open-channel configuration at a friction Reynolds number of 500 based on the channel half-height. The main goals of the paper are first to investigate the influence of the surface parameters on the mean velocity and Reynolds and dispersive stresses, particularly inside the roughness sublayer, and second to examine the possibility to parametrize the flow over irregular rough walls based on wall-normal Reynolds stresses at the plane of crests in the same way for the irregular roughness as suggested in the literature for the regular roughness. In doing so, we also examine different possible choices for the effective plane of crests.

The paper is organized in the following way. In Sec. II, the roughness generation procedure and our choice of the surface parameters is explained. In Sec. III, the numerical procedure is introduced. In Sec. IV, the simulation results from 14 rough channels as well as a smooth channel are used to investigate possible effects of roughness morphology on the outer- and inner-layer flow statistics and the quality of correlation between the roughness function and wall-normal velocity fluctuation. Section V summarizes the main findings.

II. ROUGH SURFACE

The roughness generation approach in the present paper is the same as the one in Ref. [24]. In the present section, the main aspects of this approach are summarized. The approach is based on random distribution of roughness elements of different sizes randomly on a smooth reference plane, which is the bottom boundary of the computational domain. The sizes of the roughness elements follow a random function with normal distribution within a certain variation interval. In the special case that this interval is prescribed a value of zero, all roughness elements are identical but still randomly positioned. The shape profile and the average spacing of the elements are also prescribable. Use of these tuning parameters and scaling of the geometry in wall-parallel or wall-normal directions allow adjustment of a number of surface parameters that are believed to control the problem based on the literature survey presented before. These parameters include rms roughness height k_{rms}, skewness $\mathcal{S}$ and kurtosis $\mathcal{K}$ of the surface, effective slope $\mathcal{E}$, and the coefficient of variation of peak size Δ. If k

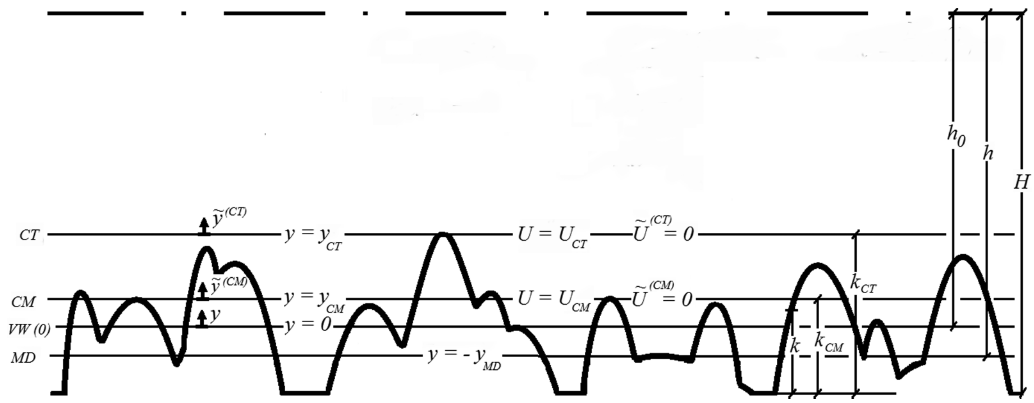

FIG. 1. Schematic representation of a rough surface: MD, meltdown plane (mean location of the surface); VW, virtual wall plane based on the best logarithmic profile fit; CM, effective plane of crests based on the mean location of all roughness peaks [k_{CM} in the figure is equal to $k_{\text{peak},ave}$ in Eq. (7)]; CT, effective plane of crests based on the location of the highest roughness peaks. Here k denotes the surface height at each point with reference to the lowest point. The dash-dotted line indicates center of the channel. In the present notation, the y coordinate has its origin at the virtual wall plane, while two other coordinate systems $\tilde{y}^{(CM)}$ and $\tilde{y}^{(CT)}$ have their origins at the CM and CT planes, respectively.

denotes the surface height measured from the bottom plane (see Fig. 1), k_{rms}, $\mathcal{S}$, $\mathcal{K}$, and $\mathcal{E}$ are defined as

$$k_{\text{rms}}^2 = \frac{1}{S}\int_S (k - k_{MD})^2 dS, \tag{2}$$

$$\mathcal{S} = \frac{1}{Sk_{\text{rms}}^3}\int_S (k - k_{MD})^3 dS, \tag{3}$$

$$\mathcal{K} = \frac{1}{Sk_{\text{rms}}^4}\int_S (k - k_{MD})^4 dS, \tag{4}$$

$$\mathcal{E} = \frac{1}{S}\int_S |\partial k/\partial x| dS, \tag{5}$$

where S is the area projected on the bottom plane and k_{MD} is the meltdown thickness defined as the mean thickness of the roughness, or

$$k_{MD} = \frac{1}{S}\int_S k\, dS. \tag{6}$$

If H is the vertical size of the computational box (open channel simulation), $h = H - k_{MD}$ will be the half-height of a smooth channel with a cross section equal to that of the rough channel under consideration. The coefficient of variation of peak size Δ is defined as a 1:50 uncertainty interval of the roughness peak sizes (Δk_{peak}) divided by the average peak size

$$\Delta = \frac{\Delta k_{\text{peak}}}{k_{\text{peak},ave}}, \tag{7}$$

where Δk_{peak} is indeed a statistical measure of the height difference between the highest and lowest peaks in the roughness.

As already discussed, in this paper we examine two possible choices for the equivalent plane of crests. The first choice is the statistical location of the highest peaks and the second is the mean location of all peaks. The former is calculated by averaging the height of the highest peaks in several area subsets, each with a size of $2h \times 2h$. We believe that this averaged maximum peak height is

TABLE I. Surface and flow parameters for all cases under investigation. The k_{rms}/h and $\mathrm{Re}_{\tau,MD}$ for all cases are 0.045 and approximately 500, respectively. Snapshots of all surfaces are presented in Appendix A. The exact definitions of $\mathrm{Re}_{\tau,0}$ and k_s^+ are in Sec. IV.

Case	Δ	$\mathcal{S}$	$\mathcal{K}$	$\mathcal{E}$	y_{MD}/h	y_{CM}/h	y_{CT}/h	$\mathrm{Re}_{\tau,0}$	k_s^+
1	0.70	0.21	2.62	0.88	0.080	0.001	0.086	460.4	121.8
2	0.35	0.21	2.57	0.88	0.087	0.035	0.085	462.2	142.6
3	0	0.21	2.58	0.88	0.111	0.048	0.048	458.2	164.2
4	0.70	0.21	2.62	0.60	0.078	0.015	0.091	468.0	115.6
5	0.70	−0.33	2.62	0.88	0.093	−0.012	0.065	471.2	75.3
6	0.35	−0.33	2.57	0.88	0.103	0.016	0.068	471.0	89.6
7	0	−0.33	2.59	0.88	0.152	0.037	0.037	468.9	99.7
8	0.70	−0.35	2.62	0.60	0.093	0.001	0.065	482.0	71.1
9	0.70	0.66	2.64	0.88	0.049	0.016	0.090	460.9	148.6
10	0.35	0.67	2.60	0.88	0.050	0.041	0.086	453.5	167.4
11	0	0.67	2.62	0.88	0.055	0.067	0.067	454.6	210.3
12	0.70	0.68	2.62	0.60	0.049	0.026	0.085	463.9	143.5
13	0.70	0.21	1.92	0.88	0.056	0.002	0.067	466.1	87.1
14	0	0.22	1.88	0.88	0.059	0.041	0.041	468.9	119.5

a more representative quantity to describe a random roughness compared to the global maximum, which only gives information about the single largest roughness peak. The size of the area subsets used for averaging is to a high extent arbitrary; here we chose the $2h \times 2h$ size as this choice leads to a satisfactory scaling of k_s based on Ref. [24]. To maintain brevity in our terminology, we use the abbreviation CT (for crest top) wherever the first choice of the effective crest is addressed and CM (for crest middle) for the second. Figure 1 illustrates different geometrical parameters related to these definitions.

Napoli *et al.* [22] and Schultz and Flack [11] classified the nonsmooth surfaces in the two categories of rough surfaces and wavy surfaces based on their effective slope. They demonstrated that in the wavy regime, where the slope is lower, the scaling between equivalent sand roughness and roughness height may not perfectly hold. For a 3D and regular roughness, a threshold of $\mathcal{E} = 0.35$ was suggested for this regime transition [11]. Later on, Yuan and Piomelli [23] suggested a higher value, $\mathcal{E} \cong 0.7$, for this threshold in random roughness. In the present paper we try to avoid the wavy regime and focus on the roughness regime; therefore, most of the investigated samples have an effective slope equal to 0.88. Apart from that, a few samples with a lower $\mathcal{E} = 0.6$ are also generated and examined to include the effect of surface slope in our parametric study. This value is slightly below the threshold suggested in Ref. [23], but considering that the regime transition is a gradual event, we believe that the waviness effect is negligible in these samples too.

The main parametric study in this paper is made on the two parameters $\mathcal{S}$ and Δ. For skewness a range of -0.4 to 0.7 is covered, which is based on the realistic surface measurements reported by Refs. [23,31,36]. Nearly 80% of all samples outlined in these references have a skewness in this range. The other key parameter Δ is varied in the range of 0–0.7. This parameter measures the departure from an idealized roughness composed of similar-size elements, i.e., the case of $\Delta = 0$. In this special case the CM and CT planes are identical. The surface parameters of the samples generated in this study and their snapshots are presented in Table I.

It is important to note that the surfaces samples covered in this study contain some important features of realistic irregular roughness, namely, randomness in size and positioning of the roughness peaks, yet cannot be considered as accurate representations of realistic roughness due to simplifications such as use of axisymmetric elements. Obviously, adding more complexity to the roughness geometry would translate to a larger degree of freedom in the geometry, thus a larger parameter space whose systematic study would only be possible with extremely high computational

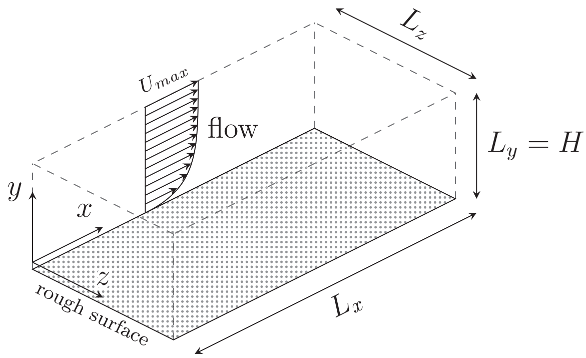

FIG. 2. Schematic of the numerical domain.

cost. The present roughness generation approach should be seen as a compromise in the complexity of the geometry to make a systematic parameter study feasible.

As a final remark on the roughness generation approach, it is important to ensure that the stochastic nature of the approach does not affect the generalizability of the results. As a matter of fact, the lateral spacing of the roughness elements in all cases is more than an order of magnitude smaller than the dimensions of the computational domain and, consequently, the number of elements is adequately large for statistically reproducible samples (the number of elements in different cases varies from 716 to 2777). Also for the first case in Table I, a second sample with all the same statistical properties is generated. The calculated statistics obtained from simulations of these two statistically identical samples match well.

The roughness generation procedure is computerized using an algorithm described in Ref. [24] and carried out during the preprocessing of the simulations and the resulting discretized surface geometry, mapped on the physical-domain solution grid, is fed into the main solver. This information is used by the solver to determine which points are located inside the solid part of the domain, on which the source term due to the immersed boundary method (IBM) should be exerted. Details of the direct forcing IBM employed in this work are explained in the following section.

III. NUMERICAL PROCEDURE

The study has been carried out using DNS of an open turbulent channel flow driven by constant pressure gradient. The implementation is based on a pseudospectral solver for incompressible boundary layer flows [37]. The Navier-Stokes equations are numerically integrated using the velocity-vorticity formulation by a spectral method with Fourier decomposition in the horizontal directions and Chebyshev discretization in the wall-normal direction. For temporal advancement, the convection and viscous terms are discretized using the third-order Runge-Kutta and Crank-Nicolson methods, respectively. Figure 2 presents the configuration of the numerical experiment with a rough surface placed at the domain lower wall and introduces a coordinate system with x, y, and z representing streamwise, wall-normal, and spanwise coordinate axes, respectively. The origin of y in the present notation is at the so-called virtual wall plane, which will be exactly defined in Sec. IV C. Periodic boundary conditions are applied in the streamwise and spanwise directions, while the wall-normal extension of the domain is bounded by no-slip boundary conditions at the lower domain boundary and symmetry boundary condition ($v = 0$ and $\partial u/\partial y = \partial w/\partial y = 0$) at the upper domain boundary.

Table II presents the properties of the numerical domain of the considered simulations. The box size of $8H \times H \times 4H$ is adopted based on Ref. [38], where it is shown that for calculation of first- and second-order one-point statistics (the ones discussed in this paper) a domain size of $2\pi H$ and πH in the streamwise and spanwise directions is sufficient up to a friction Reynolds number of at

TABLE II. Numerical domain and grid resolution of the simulations setup. Additional Fourier modes are used for 3/2-rule dealiasing in the x and z directions.

Grid size	Dimensions	Grid spacings			
$n_x \times n_y \times n_z$	$L_x \times L_y \times L_z$	Δx^+	$\Delta y^+_{\min}$	$\Delta y^+_{\max}$	Δz^+
$1152 \times 301 \times 576$	$8H \times H \times 4H$	3.65	0.015	2.7	3.65

least 2009, although some of the longest structures in the outer layer may not fit into the box. The grid spacing shown in Table II is calculated based on the average viscous length scale of all cases and can vary up to $\pm 5\%$. Statistics are calculated by integration during a time period of at least 50 turnover times after the flow has reached a statistical steady state, the turnover time being calculated for the eddies of h size and of friction velocity. This integration time corresponds approximately to 24 000 viscous time units.

The rough surface is modeled by introduction of an external volume force field to the Navier-Stokes equations based on the specific IBM proposed by Goldstein *et al.* [39]. The method imposes zero velocity in the solid region of the numerical domain utilizing a volume force distribution given by

$$F_i(x,y,z,t) = \alpha u_i(x,y,z,t) + \beta \int_0^t u_i(x,y,z,t) dt \quad \text{for } y < k(x,z), \tag{8}$$

where $k(x,z)$ is the roughness height distribution and α and β are negative constants that determine the relative strength of the applied force. This technique constitutes an explicit feedback loop in which the amount of force is determined using a direct velocity feedback and an integral feedback [first and second terms on the right-hand side of Eq. (8)]. The volume force distribution is added to the Navier-Stokes equations at every time instant of the simulation and is introduced on the dealiasing grid with additional Fourier modes (3/2 rule). Here α^{-1} and $\beta^{-1/2}$ both have the dimension of time and can be considered relaxation times of the method. Their values are tuned in the preliminary simulations. It is understood that values smaller than the viscous time scale $t_v = \nu/u_\tau^2$ lead to satisfactory results. In the present simulations values of $0.2t_v$ and $0.45t_v$ are used for the first and second relaxation times, respectively. It is worth mentioning that very low values of α and β (around an order of magnitude lower than the used values) can lead to the penetration of flow inside the solid domain, particularly around sharp corners.

To better observe the performance of the method, instantaneous snapshots of streamwise velocity field are presented in Fig. 3. In the present IBM implementation, the velocity is brought to zero only at the Cartesian grid points, which means that the interface prescribed by the IBM should pass through the grid points. This discrete interface is not perfectly smooth, as can be clearly seen in the zoomed-in snapshot. In the same figure, contours of $\pm 0.1\%$ bulk velocity are added and it is observed that the locations where the flow is brought to rest follow the prescribed surface well, although there are some minor deviations indicating that the flow slightly penetrates inside the solid body. The nonsmoothness of the captured interface is of the order of one grid spacing size, and due to the fine grid ($\Delta y^+ \approx 1$ around the tip of roughness elements) we believe that they do not influence the resulting flow; as argued in Ref. [18] the small disturbances due to IBM are likely to dissipate rapidly by viscosity and do not alter the flow in the fully rough regime where inertial drag is dominant. It is additionally observed in the zoomed-in snapshot that some spurious flow exists under the interface (bubbles formed by dotted contours). This weak flow is not expected to have an influence on the flow over roughness as it is already inside the solid domain. To confirm the sufficiency of the adopted grid resolution, a grid independence study is carried out, and it is confirmed that for the first- and second-order statistics studied in the present paper, the solution is grid independent. Also, the present implementation is validated against the high-fidelity DNS by Chan-Braun *et al.* [25], showing good agreement for the statistics of interest. Appendix B presents complementary material regarding validation and a mesh independence study.

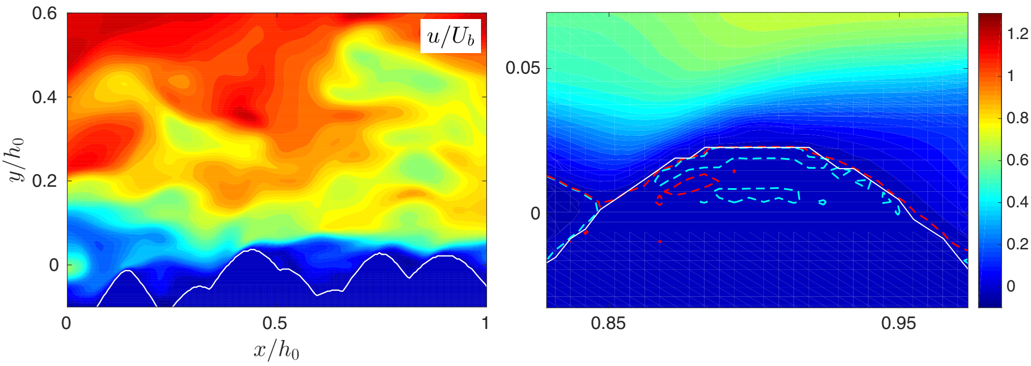

FIG. 3. Snapshots of streamwise velocity normalized by the bulk velocity over several roughness peaks (left) and a single peak (right). The white line is the desired solid surface prescribed by the IBM. Red and light blue dashed lines are the contours of $u/U_b = \pm 0.001$. The divergence of the red contour from the prescribed interface on the left-hand side of the roughness peak shown in the zoomed-in snapshot is due to the separation on the upstream peak and the resulting backflow.

IV. RESULTS AND DISCUSSION

It is a well established concept that the velocity profile over a rough wall shows a logarithmic region with a downward shift compared to the corresponding smooth wall

$$U^+ = \frac{1}{\kappa}\ln(y^+) + B - \Delta U^+. \tag{9}$$

In the present paper we adopt the same values of κ and B used by Orlandi [16] for rough channels, i.e., 0.4 and 5.5, respectively. In Eq. (9), U denotes the mean streamwise velocity. The origin of the wall-normal coordinate y for which the best logarithmic fit is obtained (referred to as the virtual wall in this paper), however, cannot be determined *a priori*. Jackson [40] proposed that the position of the virtual wall can be obtained by finding the centroid of the drag force profile due to roughness. Most researchers, however, opt for adjustment of the mean streamwise velocity profile to a logarithmic law (see Ref. [41]). In the present research we use the latter approach and determine the location of the virtual wall ($y = 0$) based on minimizing the deviation from the logarithmic law for $50 < y^+ < 150$. The locations of the meltdown plane and the two already introduced effective planes of crest relative to this origin of coordinates are $-y_{MD}$, y_{CM}, and y_{CT}, respectively (see Fig. 1). In Sec. IV C, the location of the virtual wall will be further discussed with reference to the present simulations. One can use the virtual wall to define the effective channel half-height h_0 as depicted in Fig. 1. Unlike h, h_0 is an *a posteriori* quantity.

The wall shear stress $\tau_{w,0}$ is defined by linear extrapolation of total shear stress (sum of viscous and turbulence shear stresses) from the outer region to $y = 0$, i.e., the location of the virtual wall. The method is explained in detail in Ref. [25]. Using this wall shear stress, it is possible to calculate the friction velocity $u_{\tau,0} = \sqrt{\tau_{w,0}/\rho}$ and the friction Reynolds number $\mathrm{Re}_{\tau,0} = u_{\tau,0}h_0/\nu$ for each rough channel. This friction velocity and the corresponding length scale $\nu/u_{\tau,0}$ are used to normalize the velocity U and wall distance y in Eq. (9) above. A minor disadvantage of this definition of friction Reynolds number is that it cannot be set *a priori* since the location of the virtual wall is an *a posteriori* quantity. One can, however, use h and the wall shear stress evaluated at the meltdown plane to define an alternative version of friction Reynolds number $\mathrm{Re}_{\tau,MD}$. The $\mathrm{Re}_{\tau,MD}$ is equal to 500 for all cases studied in this research, while the values of $\mathrm{Re}_{\tau,0}$ are different. These values are displayed in Table I. The values of equivalent sand roughness k_s^+ for all cases are also available in this table. Equivalent sand roughness is defined as the size of uniform sand in Nikuradse's experiment [15] resulting in the same skin friction as the surface of interest in the fully rough regime and its value in viscous units can be calculated using the definition

$$\frac{1}{\kappa}\ln(k_s^+) + B - \Delta U^+ = 8.5 \tag{10}$$

if the roughness function ΔU^+ is known [3]. Values of k_s^+ in Table I range between 71 and 210, all larger than the threshold of the fully rough regime based on a variety of works reviewed in Ref. [3]. Furthermore, for three cases 8, 9, and 13 (the two cases with the smallest k_s^+ at $\mathcal{E} = 0.88$ and the one at $\mathcal{E} = 0.6$), extra simulations at $\mathrm{Re}_{\tau,0} \cong 420$ and 570 are carried out and the logarithmic relation of the roughness function with the characteristic roughness size in wall units is confirmed. The extra simulations at the highest Reynolds number are carried out using 1.5 times more grid points in the wall-normal direction to ensure a satisfactory grid resolution.

Fluctuating velocity components are obtained by subtracting the temporally averaged velocity at each point from the instantaneous velocity at the same point

$$u_i'(x,y,z,t) = u_i(x,y,z,t) - \overline{u}_i(x,y,z). \tag{11}$$

An overline indicates temporal averaging. Unlike in a smooth channel, in a rough one, the time-averaged velocity $\overline{u}_i$ varies in a wall-parallel plane, particularly in the region close to or below the roughness peaks. We calculate the difference between $\overline{u}_i$ at each (x,y,z) location and $\langle\overline{u}_i\rangle$ additionally averaged over the xz plane at the same y in order to obtain a local velocity difference, which is indicated with a circumflex,

$$\hat{u}_i(x,y,z) = \overline{u}_i(x,y,z) - \langle\overline{u}_i\rangle(y). \tag{12}$$

In the following, angular brackets indicate area averaging over the y-normal plane. Indeed, $\hat{u}_i$ measures the spatial inhomogeneity of the time-averaged velocity field $\overline{u_i}$. For brevity, double-averaged velocity components $\langle\overline{u}_{1,2,3}\rangle$ are denoted by capital letters U, V, W, or U_i hereinafter.

Reynolds stresses are the temporal average of the products of fluctuating velocity components defined by Eq. (11), i.e., $\overline{u_i'u_j'}$. Analogous to Reynolds stresses, dispersive stresses can be calculated by spatially averaging the products of the $\hat{u}_i$ velocity differences defined by Eq. (12), i.e., $\langle\hat{u}_i\hat{u}_j\rangle$. It should be noted that dispersive stresses $\langle\hat{u}_i\hat{u}_j\rangle$ are only functions of the y coordinate, while Reynolds stresses $\overline{u_i'u_j'}$ are functions of all three coordinates in space. Although the Reynolds and dispersive stresses are analogous in definition, they are different in nature; the former measures the local momentum transfer due to turbulence fluctuations, while the latter measures the momentum transfer in a given wall-parallel plane due to geometry-induced spatial inhomogeneity.

It can be shown that the difference between the local instantaneous velocity u_i and the double-averaged velocity U_i is equal to the sum of u_i' and $\hat{u}_i$. This velocity difference is indicated by a double prime in the present notation,

$$u_i''(x,y,z,t) = u_i(x,y,z,t) - U_i(y) = u_i'(x,y,z,t) + \hat{u}_i(x,y,z). \tag{13}$$

In consequence, the sum of Reynolds and dispersive stresses can be expressed in terms of the u_i'' products

$$\langle\overline{u_i''u_j''}\rangle = \langle\overline{u_i'u_j'}\rangle + \langle\hat{u}_i\hat{u}_j\rangle, \tag{14}$$

where $\langle\overline{u_i'u_j'}\rangle$, being a function of y only, is the Reynolds stress additionally averaged in the y-normal plane. In a smooth channel where the time-averaged flow is homogeneous parallel to the wall, there is no distinction between $\langle\overline{u_i''u_j''}\rangle$ and $\langle\overline{u_i'u_j'}\rangle$. In rough channels, as Eq. (14) suggests, their difference corresponds to the dispersive stress $\langle\hat{u}_i\hat{u}_j\rangle$.

As mentioned above, Reynolds stress $\overline{u_i'u_j'}$ is, in the general case, a function of all space coordinates. The present results suggest that in the flow over a rough wall, Reynolds stresses can be significantly inhomogeneous in the wall parallel directions up to a certain wall distance. To better observe this inhomogeneity, fields of all Reynolds stress components for one simulated case on a z-normal plane are presented in Fig. 4. The time-averaged streamwise velocity on the same

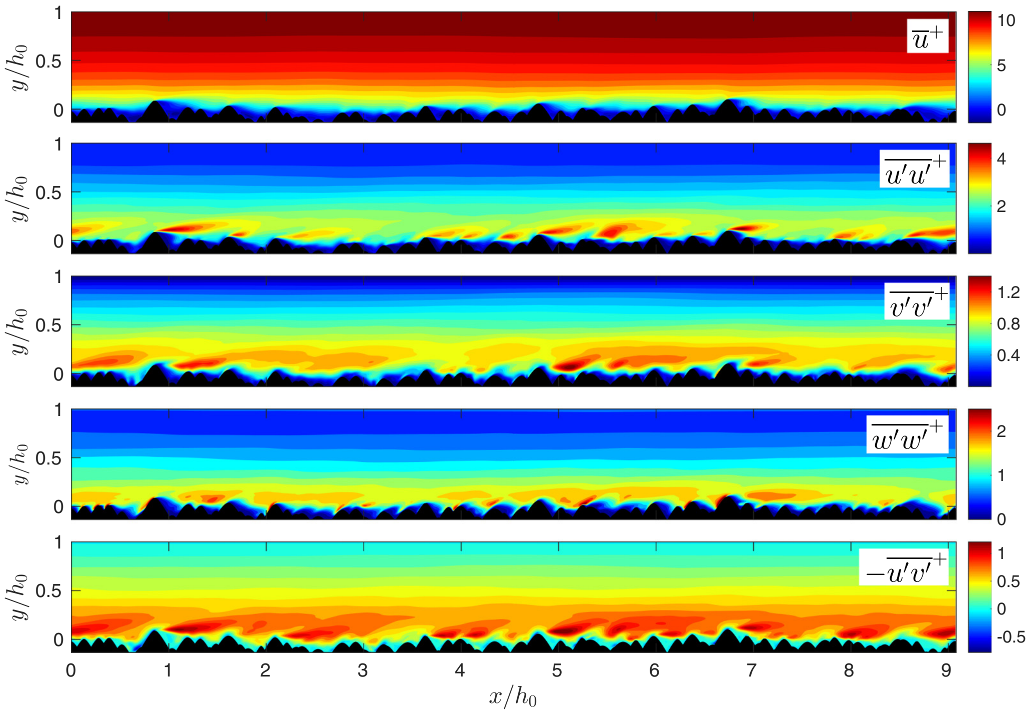

FIG. 4. Time-averaged streamwise velocity (top row); streamwise (second row), wall-normal (third row), and spanwise (fourth row) normal Reynolds stresses; and Reynolds shear stress (bottom row) for case 1 in an arbitrary z plane. All field variables are normalized with $u_{\tau,0}$ or $u^2_{\tau,0}$.

plane is also displayed in the top plot of this figure, where it can be seen that the isocontours are roughly parallel to the wall at a short distance above the highest roughness peaks. As for the Reynolds stresses, the parallel isocontours start to be present at higher distances above the roughness peaks, i.e., roughly at $y/h_0 = 0.4$. Parallel isocontours obviously indicate homogeneity in the x direction. Near the roughness peaks, however, all Reynolds stresses are highly inhomogeneous in the x direction. For instance, $\overline{v'v'}^+$ can locally reach values above 1.3, which is about 30% higher than the peak value of its xz-averaged profile, which, as will be discussed later, approximately equals unity. It is also observed in Fig. 4 that both streamwise and wall-parallel Reynolds stresses as well as the Reynolds shear stress reach their highest values (dark red color) in the regions downstream of the highest roughness peaks, which is most likely a sign of mixing due to vortex shedding past these peaks.

Quantitative discussion of the flow statistics in the outer and inner layers for all the simulated cases follows in Secs. IV A and IV B. In Sec. IV C the logarithmic law of the wall and its different versions for a rough channel are discussed. Finally, in Sec. IV D, parametrization of roughness using wall-normal velocity fluctuation will be examined.

A. Outer-layer similarity

Investigation of outer-layer similarity begins with a comparison of double-averaged profiles of first- and second-order one-point statistics. Figure 5 compares these profiles for all 14 simulated cases. The top two plots depict the defect of the mean velocity profile $U^+(y/h_0)$ with reference to its value at the center of the channel $U^+_{\max}$. The bottom two plots depict diagonal components of the $\langle\overline{u''_i u''_j}\rangle^+$ tensor and the shear stress. The statistical location of the highest roughness peaks (CT) is

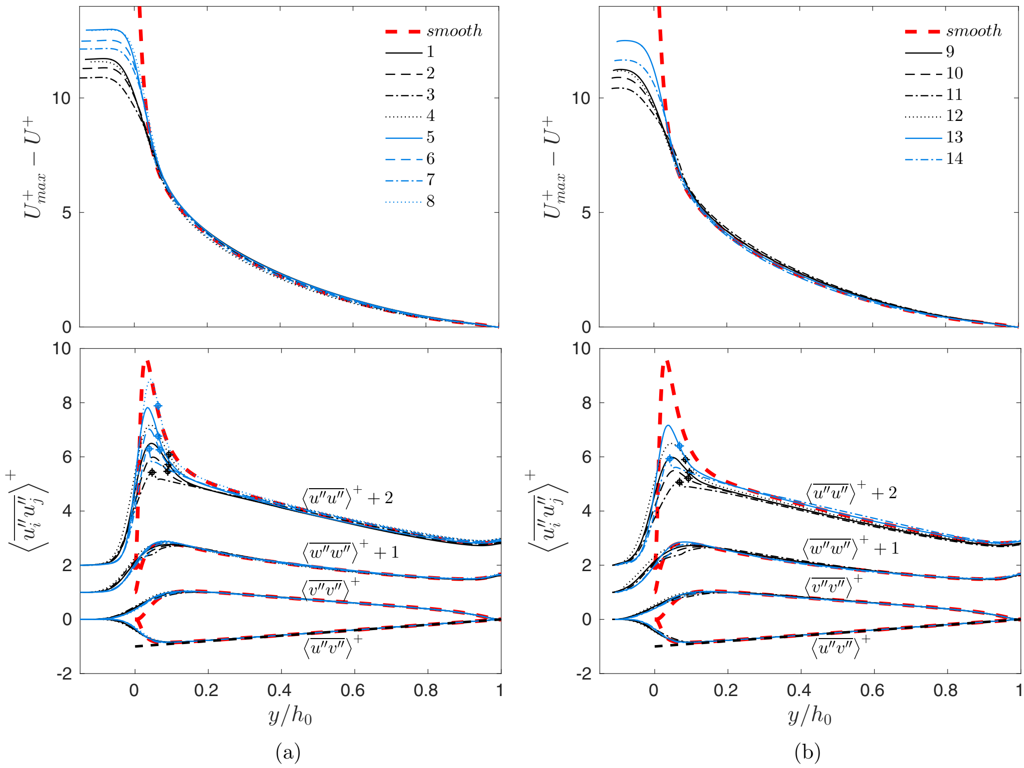

FIG. 5. Mean streamwise velocity defect profiles (top) and the sum of Reynolds and dispersive stress profiles (bottom) of all simulated cases against outer scale wall distance. For clarity, $\langle \overline{w''w''} \rangle^+$ and $\langle \overline{u''u''} \rangle^+$ curves are shifted upward by one and two units, respectively (similarly for the smooth curve). Numbers in the line legend correspond to the case numbers in Table I. The symbols on $\langle \overline{u''u''} \rangle^+$ curves indicate the locations of the highest peaks in the respective samples.

shown by a symbol on one curve for each case. Interestingly, the mean velocity profiles in Fig. 5 demonstrate a nearly perfect similarity down to the very vicinity of the roughness peaks. Also, the Reynolds stress profiles collapse within a $\pm 3.5\%$ difference once y/h_0 is greater than roughly 0.3. Minor wall-parallel inhomogeneities that may exist at higher locations (see Fig. 4) are smoothened out due to spatial averaging. The $\pm 3.5\%$ discrepancy among different curves that continues to exist up to the center of the channel can possibly be an indication of the low-Reynolds-number effects. A similar minor mismatch is also observed in the center of the channel by Thakkar *et al.* [31] in their DNS of channels with two rough walls at $\mathrm{Re}_\tau = 180$. This mismatch is most pronounced for the streamwise component. Obviously, the wall-normal component is always zero in the middle of the channel due to the impermeability boundary condition applied. The profiles of shear stress $\langle \overline{u''v''} \rangle^+$ for all rough and smooth channels collapse perfectly with the linear relation (shown by a thick dashed line) until the very vicinity of the wall. It must be noted that, as will be shown later, dispersive stresses are negligible compared to the Reynolds stresses outside the roughness sublayer; therefore, although here the profiles of $\langle \overline{u_i'' u_j''} \rangle^+$ are used as the proof of outer-layer similarity, the same conclusion would be achieved for $\langle \overline{u_i' u_j'} \rangle^+$.

Figures 6(a) and 6(b) show the variation of local u_{rms}/U as a function of U/U_{max}, where u_{rms} is the square root of $\langle \overline{u''u''} \rangle$. This type of diagnostic plot is suggested by Alfredson *et al.* [42] and experimentally shown to be universal in the outer layer at least for smooth-wall-bounded turbulence at adequately large Reynolds numbers. As observed in the figure, the present smooth channel results

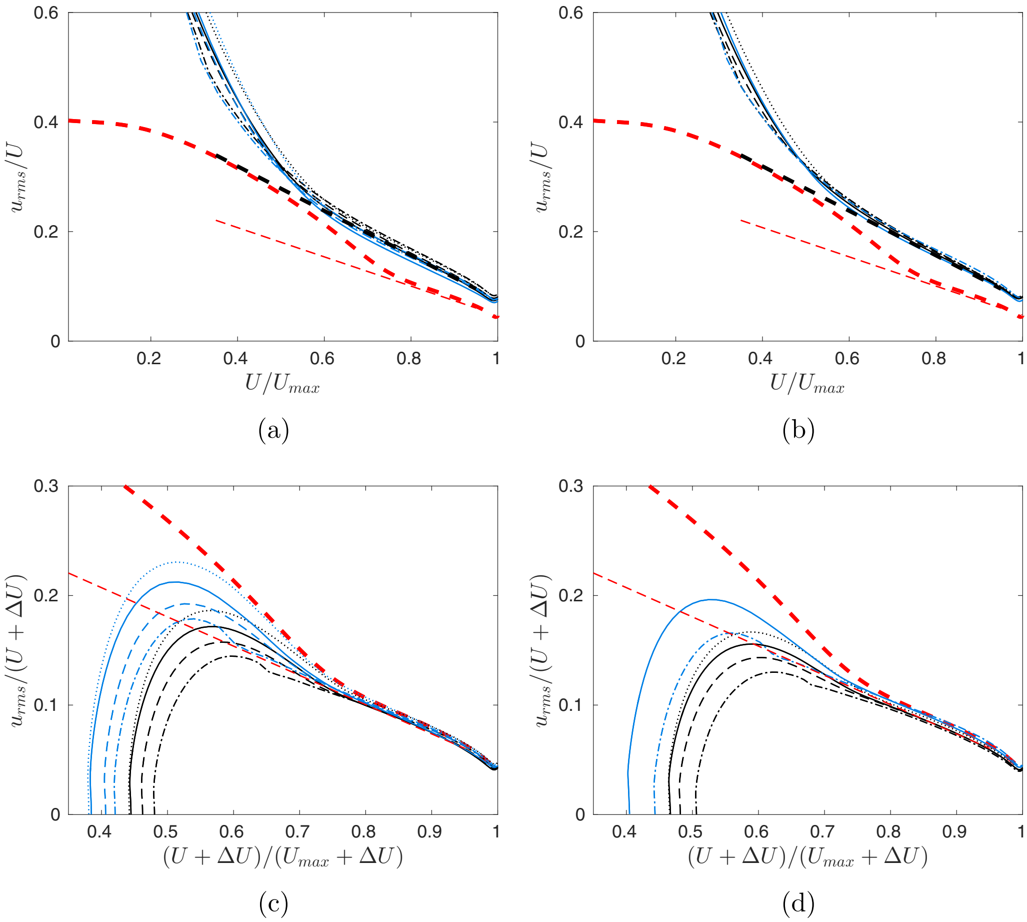

FIG. 6. (a) and (b) Streamwise turbulence intensity u_{rms}/U as a function of local normalized mean velocity $U/U_{\max}$ for all simulated cases as well as the smooth channel at $\mathrm{Re}_\tau = 500$. The line legend is the same as in Fig. 5. The red and black dashed lines represent the linear relation set by Eq. (15) with $(a,b) = (0.314,-0.267)$ and $(0.482,-0.407)$, respectively. (c) and (d) Same profiles obtained when U is replaced by $U + \Delta U$.

collapse into the linear relation

$$\left(\frac{u_{\mathrm{rms}}}{U}\right) = a + b\left(\frac{U}{U_{\max}}\right) \tag{15}$$

when $U/U_{\max} > 0.75$ if the constants suggested by Ref. [43] for the channel flow ($a = 0.314$ and $b = -0.267$) are applied. It is however revealed by the same plot that the rough curves do not collapse into the same relation as the smooth channel, but into another linear relation ($a = 0.482$ and $b = -0.407$). This is in accordance with the findings by Castro *et al.* [44]. These authors proposed that a more general scaling than that of Eq. (15) is required when ΔU^+ is nonzero and obtained a universal collapse among the smooth and rough zero-pressure-gradient turbulent boundary layer results by using a modified diagnostic plot in which U^+ is replaced by $U^+ + \Delta U^+$. The modified diagnostic plots for the present data are provided in Figs. 6(c) and 6(d) and the same universal behavior is observed for the present channel result. The extent of the linear region of the present profiles is shorter than that reported in Ref. [44], which is likely a low-Reynolds-number effect.

A common way to define the extent of the roughness sublayer is by taking the wall-normal location where the mean profiles of turbulence statistics collapse into those of the corresponding smooth wall as the edge of the roughness sublayer [7]. Based on the statistics of second order for the cases studied in the present paper (Fig. 5), the roughness layer terminates at $y/h_0 = 0.3$ or in viscous units $y^+ \approx 150$. It should be kept in mind that, in the present notation, y measures the distance from the virtual wall plane and not the bottom plane. In the literature the extent of the roughness sublayer is often expressed in terms of the depth of the sublayer from the bottom plane and normalized by the roughness height. For the present cases this definition leads to a roughness sublayer extent of $2k_z$–$2.7k_z$, where k_z is the statistical size of the highest roughness peaks (precisely defined as the vertical distance between the CT plane and the bottom plane). An alternative, and more general, definition for the roughness sublayer is the layer where the turbulence statistics are inhomogeneous due to the presence of roughness [27]. This definition shifts the edge of roughness sublayer farther away from the wall for the present results and leads to roughness sublayer depths as large as $2.6k_z$–$3.7k_z$ based on second-order statistics, i.e., Reynolds stresses. It is clear from Figs. 4 and 5 that if the first-order statistics, i.e., mean velocity profiles, are used for the definition of the roughness sublayer, either definition would lead to a smaller roughness sublayer as the effect of roughness on the mean velocity fades out in a shorter distance above the roughness peaks than on the Reynolds stresses.

B. Reynolds and dispersive stresses in the roughness sublayer

Figure 7 compares the profiles of Reynolds and dispersive stresses (the three normal stresses as well as the shear stress) normalized with the wall shear stress of the corresponding case $\tau_{w,0}$. To maintain the clarity of the graphs and avoid prolonging the paper, only profiles of four representative cases (5, 7, 9, and 11) are shown in this figure. These cases feature a combination of the highest and lowest values of $\mathcal{S}$ and the highest and lowest values of Δ simulated in this research. In view of the fact that profiles of $\langle \overline{u_i'' u_j''} \rangle^+$ are already investigated for the whole cross section, in the present section of the paper, only the statistics in the vicinity of the roughness crest, i.e., $y/h_0 < 0.3$, are shown. The first notable observation in Fig. 7 is that, except for the streamwise component, dispersive stresses are considerably smaller than the Reynolds stresses. For the wall-normal component, in particular, the dispersive stress is almost negligible. Considering all cases studied in this paper, the ratios of the peak dispersive stress value to the peak Reynolds stress value are less than 10%, 23%, and 21% for the vertical, spanwise, and shear components, respectively. This ratio is depicted for the streamwise component against Δ in Fig. 8. In order to include information regarding other geometrical parameters in the same figure, different symbol shapes and sizes are used for different values of $\mathcal{S}$ and $\mathcal{E}$ (see the figure caption). Clear trends with geometrical parameters can be observed in Fig. 8. Dispersive stresses become relatively large with an increase in Δ but a decrease in $\mathcal{E}$. High streamwise dispersive stresses indicate inhomogeneity of mean velocity in the y-normal planes caused by the roughness elements. This inhomogeneity can increase by a decrease in the mean roughness slope as a lower slope translates to more sparsely distributed roughness peaks with more distinguished wakes, hence an increase in the streamwise dispersive stress. The same argument holds for an increase in Δ as it leads to larger distances among the highest roughness peaks or, in other words, a sparser roughness close to the top crest where the peak in dispersive stresses is observed. It is also observed (not shown here) that the sum of dispersive and Reynolds stresses also increases with a decrease in the slope and an increase in Δ. This trend is in qualitative agreement with findings of previous studies on the effect of the roughness slope on turbulence statistics [31,34].

Another observation in Fig. 7 is that peak values of $\langle \overline{u_i' u_j'} \rangle^+$ for different rough cases lie relatively close to each other. Figure 9 makes possible a comparison of the peak values of Reynolds stresses against that of a smooth channel at $\mathrm{Re}_\tau = 500$. In this figure the values of Reynolds stresses are normalized once with $\tau_{w,0}$ and once with the square of the respective bulk velocity U_{bulk}^2. The bulk velocity is defined as the volumetric flow rate divided by the cross-sectional area. When normalization with $\tau_{w,0}$ is applied, the vertical bars in the figure, indicating the range of values in all simulated rough

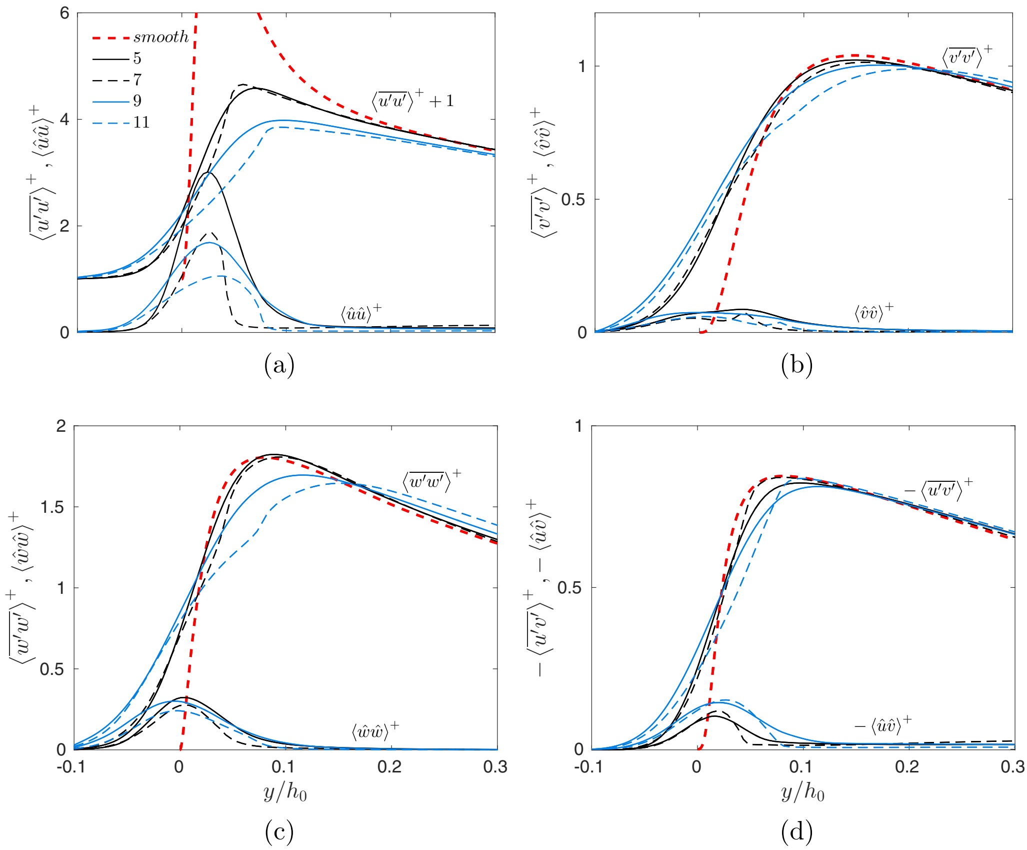

FIG. 7. Profiles of spatially averaged Reynolds stresses and dispersive stresses normalized with wall shear stress $\tau_{w,0}$ for cases 5, 7, 9, and 11 in Table I as well as the smooth channel at $\mathrm{Re}_\tau = 500$. The smooth channel profiles are the same as in Fig. 5; therefore, the peak of the smooth profile in (a) is excluded to keep the clarity of the other profiles.

channel cases, are very small. It can be concluded that the roughness morphology does not interfere with the scaling of peak Reynolds stresses in viscous units. Only the streamwise component shows some sensitivity to the morphology. Interestingly, the inner-scaled peak values of the spanwise and wall-normal stresses are very similar to the smooth wall while the streamwise stress is significantly damped over the rough wall. This damping has already been reported by several authors [23,33] and related to the suppression of elongated near-wall structures due to roughness. The similar peak values of $\langle \overline{v'v'} \rangle^+$ and $\langle \overline{w'w'} \rangle^+$ for the smooth and all rough cases are a notable observation. It is important to understand if this scaling is universal or, for example, shows a Reynolds-number dependence. Due to the limited computational capacity, the present study is limited to the effects of geometry and cannot be extended to the effect of Reynolds number. It is however possible to obtain some insight from the previous works. Busse *et al.* [32] and Yuan and Piomelli [23] conducted a rough channel DNS (highly resolved LES in the latter case) at friction Reynolds numbers of 180 and 1000, respectively, which complements the present results well. The former authors reported very similar peak values of $\langle \overline{v'v'} \rangle^+$ and $\langle \overline{w'w'} \rangle^+$ for a smooth and a rough channel. The latter authors investigated a number of different roughness geometries and observed that the peak values of $\langle \overline{v'v'} \rangle^+$ for the rough channels are 10%–25% smaller than those in the smooth channel, while the peak values of $\langle \overline{w'w'} \rangle^+$ for the rough channels are within $\pm 10\%$ of the smooth case (all percentages are approximate). These results, along with the ones presented in this paper, suggest that the discussed inner scaling may be altered

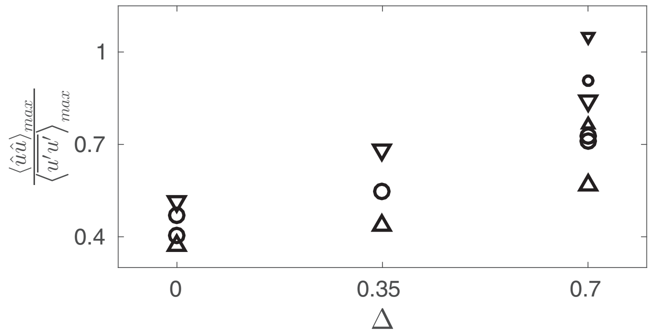

FIG. 8. Ratio of maximum dispersive stress to maximum Reynolds stress for all simulated cases against Δ. Different symbol types indicate different values of skewness: $\triangledown$, $\mathcal{S} \cong -0.33$; $\bigcirc$, $\mathcal{S} \cong 0.21$; and $\triangle$, $\mathcal{S} \cong 0.67$. Smaller symbols indicate the cases with smaller values of $\mathcal{E}$ (=0.6).

for higher Reynolds numbers, more likely for the wall-normal component, but this sensitivity to the Reynolds number is relatively low.

Figure 9(b) shows that when the peak values of the Reynolds stresses are scaled in outer units, i.e., with the bulk velocity, the results from the rough channels are meaningfully larger than for a smooth channel. As a matter of fact, all simulations are run at the same friction Reynolds number, which means that U_{bulk} decreases due to the roughness and consequently the peak Reynolds stress normalized by U_{bulk}^2 increases. The increase in the Reynolds stress normalized by U_{bulk}^2 can be seen as an increase in the turbulent kinetic energy relative to the mean kinetic energy caused by roughness.

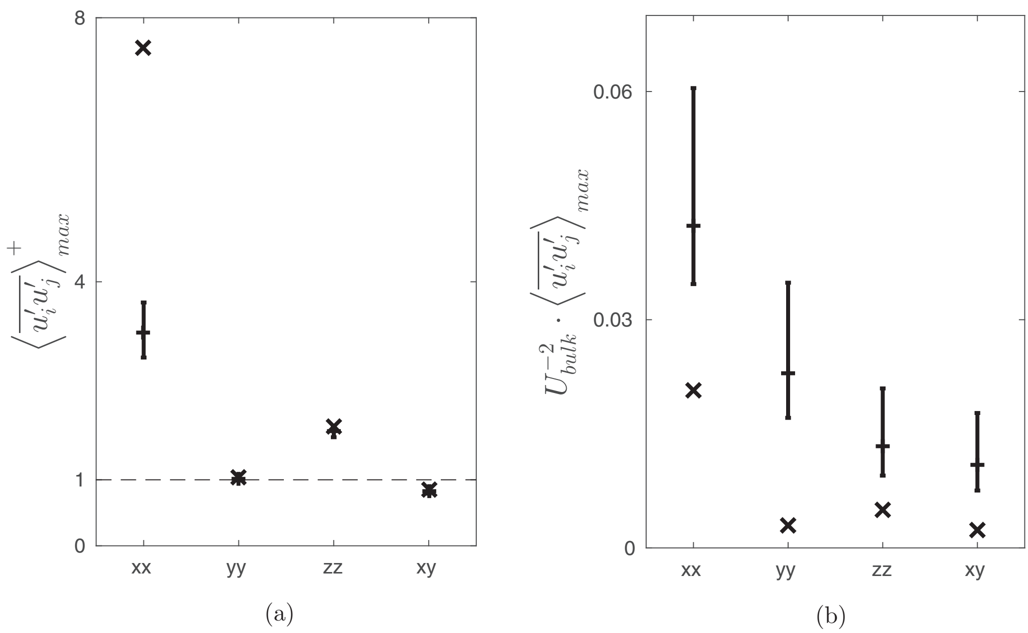

FIG. 9. Peak values of Reynolds stresses from rough channel simulations (vertical bars) compared with the smooth channel at $\mathrm{Re}_\tau = 500$ (crosses). The bars indicate the range of values obtained for all simulated cases. (a) Reynolds stresses are normalized with wall shear stress $u_{\tau,0}$. (b) Reynolds stresses are normalized with square bulk velocity in the channel.

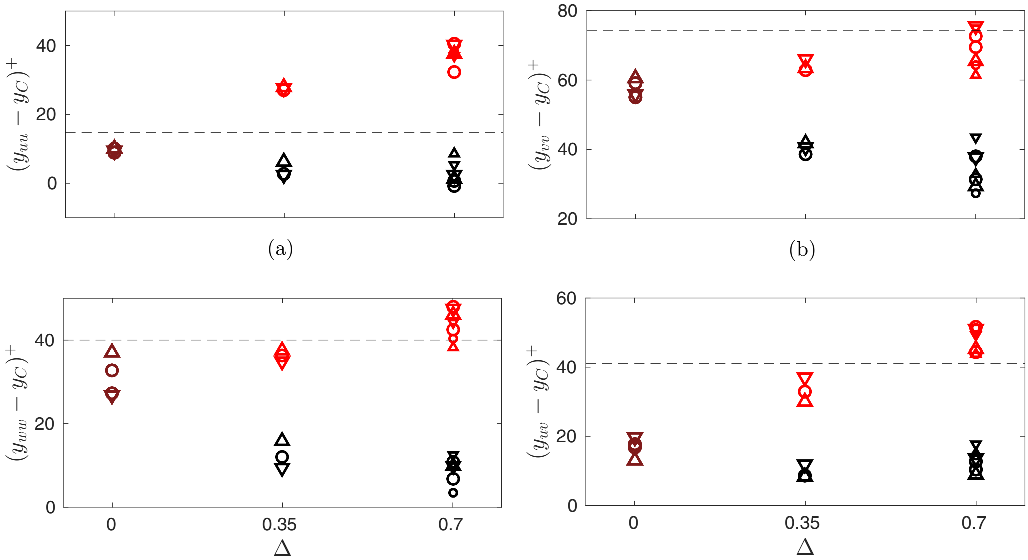

FIG. 10. Peak locations of (a) $\langle\overline{u'u'}\rangle$, (b) $\langle\overline{v'v'}\rangle$, (c) $\langle\overline{w'w'}\rangle$, and (d) $\langle\overline{u'v'}\rangle$ against Δ for all simulated cases. The abscissa shows the peak location with reference to the coordinate attached to the effective crest of the plane ($C \equiv CM$ or CT). For black symbols $C \equiv CT$ and for red symbols $C \equiv CM$. The cases with $\Delta = 0$, in which $C \equiv CT \equiv CM$, are shown using brown symbols. Different symbol types indicate different values of skewness: $\bigtriangledown$, $\mathcal{S} \cong -0.33$; $\bigcirc$, $\mathcal{S} \cong 0.21$; and $\triangle$, $\mathcal{S} \cong 0.67$. Smaller symbols indicate the cases with smaller values of $\mathcal{E}$ (=0.6). The horizontal dashed lines indicate the peak locations above the wall for the smooth channel at $\mathrm{Re}_\tau = 500$.

Unlike in Fig. 9(a), large vertical bars are obtained for all components in Fig. 9(b) as the peak Reynolds stresses do not scale in outer units.

The last point to be discussed regarding the double-averaged profiles of Reynolds stresses is the y^+ distance at which the profiles peak. Of particular interest are the distances of the peak locations from the roughness crest. To avoid confusion due to frequent reference to peaks in Reynolds stress and peaks of rough surface in the text, we always refer to the latter as the roughness peaks. Figure 10 shows the peak locations of the four Reynolds stress components discussed above for all 14 simulated cases as a function of Δ. In this figure (and all similar figures throughout the paper) black symbols are used to indicate the plane of crests based on the highest roughness peaks ($C \equiv CT$) and red symbols are used to indicate the plane of crests based on the mean location of roughness peaks ($C \equiv CM$). If $\Delta = 0$ the two planes are identical, and the corresponding data points are shown using brown symbols. The peak locations for the smooth channel, measured from the wall, are also given in the same figures using horizontal dashed lines. It is clearly shown that with an increase in Δ, all $(y - y_{CM})^+$ values increase while all $(y - y_{CT})^+$ values decrease. In other words, comparing a surface with dissimilar roughness elements to one with similar roughness elements, the peaks of Reynolds stresses are closer to the CT but farther from the CM plane.

Considering the streamwise normal component, its maximum is always at a roughly constant y^+ distance (0–10) above the CT plane, which is lower but still comparable to the wall distance of the $\langle\overline{u'u'}\rangle$ peak in a smooth case. For the Reynolds shear stress, similarly, the peak has an approximately constant y^+ distance from the CT plane, but the distance is considerably lower than in the smooth case. Regarding the other two normal components of the Reynolds stress, the variation of $(y - y_{CM})^+$ with Δ is less steep than that of $(y - y_{CT})^+$, which can indicate that these components adjust themselves more to the CM plane rather than the CT plane. For the vertical normal component, the $(y - y_{CM})^+$

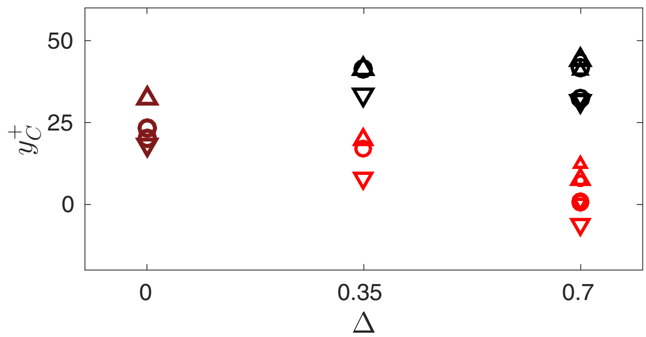

FIG. 11. Wall-normal location of the effective crest of the plane with reference to the virtual wall for all simulated cases against Δ. Symbols have the same meaning as in Fig. 10.

locations of the peaks vary from 55 to 75 viscous units, i.e., 20 to 0 viscous units lower than that of the smooth channel.

C. Logarithmic law of the wall

Equation (9) defines the logarithmic law of the wall for a rough wall. As already discussed, the origin of the y coordinate has to be determined *a posteriori*. This serves as a motivation to define an alternative version of the law of the wall for rough walls, in which the origin of coordinate can be determined merely based on the geometry. Orlandi and Leonardi [18,19] proposed such an alternative form for expressing the mean velocity profile in which the origin of coordinates is shifted to the plane of the crests. The wall-normal coordinate and mean streamwise velocity in the new formulation are defined as

$$\tilde{y}^{(C)} = y - y_C, \tag{16}$$

$$\tilde{U}^{(C)}(y) = U(y) - U_C, \tag{17}$$

where U_C denotes the value of U at the plane of crests. In the present paper we follow Refs. [18,19] in using the tilde to indicate the wall-normal coordinate with reference to the plane of crests and the corresponding velocity. We additionally use a superscript to specify which definition of the crest of planes is used [$(C) \equiv (CM)$ or (CT)]. The new velocity and wall distance can be normalized in viscous units as

$$\tilde{y}^{(C)+} = \frac{\tilde{y}^{(C)} u_{\tau,C}}{\nu}, \quad \tilde{U}^{(C)+} = \frac{\tilde{U}^{(C)}}{u_{\tau,C}}, \tag{18}$$

where $u_{\tau,C}$ is the the friction velocity based on the total shear stress evaluated at $y = y_C$ instead of $y = 0$. Using the new variables, the logarithmic law of the wall over a rough wall can be expressed as

$$\tilde{U}^{(C)+} = \frac{1}{\kappa}\ln(\tilde{y}^{(C)+}) + B - \Delta\tilde{U}_C^+. \tag{19}$$

The new formulation can also be considered as a more direct analogy of the velocity profile over smooth walls as, by definition, $\tilde{U}^{(C)+}|_{\tilde{y}^{(C)+}=0} = 0$. Obviously, the roughness function $\Delta\tilde{U}_C^+$ in the new formulation is different from ΔU^+ in Eq. (9).

In the present section, all three variants of the law of the wall (the conventional definition and the alternative one with two choices of the plane of crests) are presented. It is however insightful to first pay some attention to the location of the virtual wall relative to the two effective planes of crests. For this purpose, the values of y_C^+ for all cases are plotted against Δ in Fig. 11. It is observed in Fig. 11

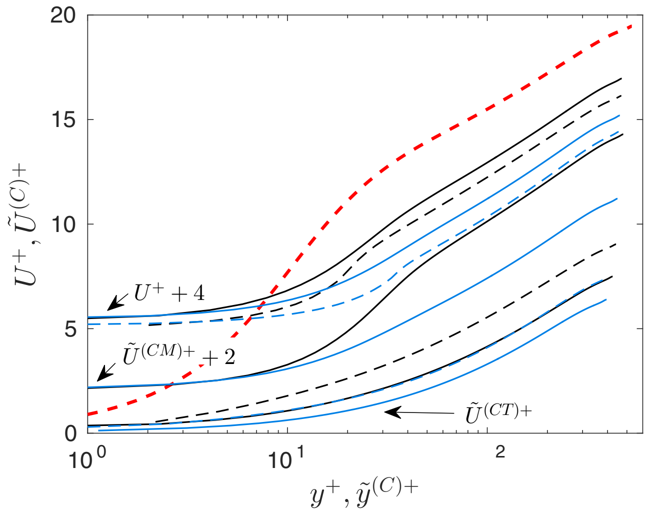

FIG. 12. Mean streamwise velocity profiles of four representative cases (5, 7, 9, and 11). The abscissa variable is y^+, $\tilde{y}^{(CM)+}$, or $\tilde{y}^{(CT)+}$ for different groups of curves. The ordinate variable is U^+, $\tilde{U}^{(CM)+}$, or $\tilde{U}^{(CT)+}$ for the respective groups of curves. For clarity, the U^+ and $\tilde{U}^{(CM)+}$ curves are shifted upward by four and two units, respectively, and the curve for the smooth case is shifted downward by the logarithmic-law intercept value B. The line legend is the same as in Fig. 7. For the cases 7 and 11, $\tilde{U}^{(CM)+}$ and $\tilde{U}^{(CT)+}$ are the same, hence only of the two is plotted.

that for a fixed $\mathcal{S}$, y_{CT} does not show strong variations with Δ. In other words, the virtual wall adjusts itself more or less to the location of the highest roughness peaks. Obviously, with an increase in Δ, the difference between y_{CT} and y_{CM} grows and hence y_{CM} decreases. Another general trend observed in the figure is that y_C increases slightly but consistently with $\mathcal{S}$. Recalling the correspondence between the virtual wall and the centroid of drag profile, it can be said that the drag due to the positively skewed rough surface occurs at deeper locations, i.e., lower y positions with respect to the roughness crest.

Figure 12 shows the mean velocity profiles of the four representative cases in inner-logarithmic scales in comparison with the profile of a smooth channel at $\mathrm{Re}_\tau = 500$. It is observed that when the conventional $U^+(y^+)$ formulation is used, all curves show a clear logarithmic region roughly in the range of $y^+ = 50$–300. Expectedly, with a shift in the origin of the y coordinate in the $\tilde{U}^+(\tilde{y}^+)$ formulations, the same logarithmic behavior cannot be repeated. In particular, when $C \equiv CT$, the logarithmic region becomes smaller and starts at a higher distance from the wall [compare to Fig. 2(a) in Ref. [16]]. This can be seen as a disadvantage of using Eq. (19) instead of Eq. (9) for the law of the wall, in particular at low Reynolds numbers, as the plane of crests does not necessarily coincide with the virtual wall. There is, however, still a satisfactory logarithmic behavior in the range of $\tilde{y}^{(CT)+} = 150$–250 which allows the calculation of the roughness function.

D. Parametrization of the roughness using $v^+_{\mathrm{rms}}|_{y_C}$

A major goal of this paper is to investigate the correlation between the wall-normal fluctuating velocity

$$v^+_{\mathrm{rms}}|_{y_C} = \frac{[\langle \overline{v'v'} \rangle_{(\tilde{y}^{(C)}=0)}]^{1/2}}{u_{\tau,C}} \tag{20}$$

and the roughness function $\Delta \tilde{U}^+_C$. As before, the superscript or subscript C can be replaced by either CT or CM depending on which definition of the effective plane of crests is adopted.

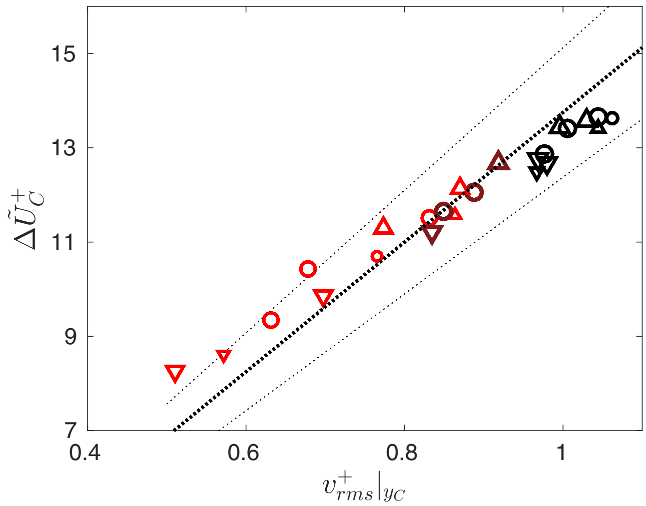

FIG. 13. Correlation between the roughness function and wall-normal fluctuating velocity $v^+_{\mathrm{rms}}|_{y_C}$ at the effective plane of crests for all simulated cases using two definitions of an effective plane of crests ($C \equiv CM$ or CT). Symbols have the same meaning as in Fig. 10. Dotted lines indicate Eq. (1) and its $\pm 10\%$ deviation.

Figure 13 depicts the values of roughness function obtained from all simulated cases as a function of $v^+_{\mathrm{rms}}|_{y_C}$. Similar to Figs. 10 and 11, red and black symbols are used to distinguish the two definitions of the effective plane of crests (CM and CT). The thick dotted line indicates the linear relation suggested by Orlandi and Leonardi [18,19], i.e., Eq. (1). It is observed that, generally speaking, the trend of the roughness function is predicted by the linear relation. To facilitate visual comparison, thin dotted lines corresponding to $\pm 10\%$ deviation from Eq. (1) are also plotted in the same figure. While almost all data points lie within this deviation, there is a downward (upward) shift for black (red) symbols. Interestingly, the symbols corresponding to $\Delta = 0$ show a very good match with the linear relation. This may be an indication that the linear relation indeed is most appropriate for a roughness with similar elements, the kind of roughness for which this relation was originally obtained by Orlandi and Leonardi. For a roughness with dissimilar elements ($\Delta > 0$), even though the linear correlation is still a good approximation, there is some uncertainty due to the lack of a clear-cut plane of the crest. When the CT plane is chosen as the crest, DNS data show a smaller roughness function at the same $v^+_{\mathrm{rms}}|_{y_C}$ or a larger $v^+_{\mathrm{rms}}|_{y_C}$ at the same roughness function, and when the CM plane is used vice versa. This systematic overprediction or underprediction suggests that one may be able to find an effective crest plane between the CM and CT planes, which delivers similarly good collapse for $\Delta > 0$ as for $\Delta = 0$. Nevertheless, for the time being, we do not further examine this possibility.

It is important to note that despite the imperfect collapse of the data points in Fig. 13, the correlation of the roughness function with wall-normal turbulent fluctuations is far better than what can be achieved using any of the geometrical surface parameters, namely, skewness, effective slope, and Δ (see Ref. [24] for a full discussion of the geometrical parametrization of roughness). This suggests that the roughness function is physically more closely linked to $v^+_{\mathrm{rms}}|_{y_C}$ than the surface statistics, although as a predictive quantity it has the disadvantage of not being *a priori*.

As mentioned before, the use of the alternative formulation for the logarithmic law of the wall, i.e., Eq. (19), rules out the need to determine the location of the virtual wall, but at the same time requires the determination of another *a posteriori* quantity, the mean streamwise velocity U_C^+ at the plane of crests. The parametrization based on wall-normal turbulent fluctuations is hence more complete if this quantity can be correlated to $v^+_{\mathrm{rms}}|_{y_C}$. Figure 14 is presented to examine such a correlation. The figure reveals that there is indeed some general correlation between the two quantities, at least when

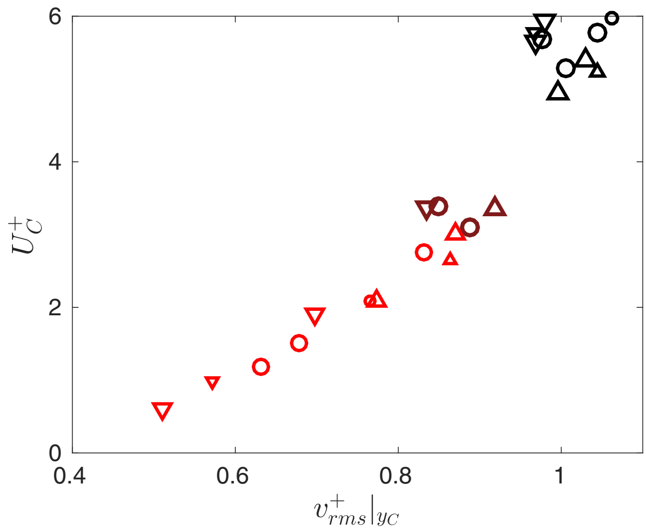

FIG. 14. Correlation between the mean streamwise velocity and wall-normal fluctuating velocity $v^+_{\text{rms}}|_{y_C}$ at the effective plane of crests for all simulated cases using two definitions of an effective plane of crests ($C \equiv CM$ or CT). Symbols have the same meaning as in Fig. 10.

the CM definition is used. For the CT plane the correlation is not convincing. A possible explanation can be that the CT plane is already fairly close to the edge of the roughness sublayer (see Fig. 5, where the mean velocity defect profiles show a collapse very close to the location of the highest peaks). This means that the velocity at this plane is more directly controlled by the outer-layer velocity and therefore the inner scaling of U_{CT} does not meaningfully reflect the variation in the roughness function.

Relying on one quantity directly arising from the turbulent flow ($v^+_{\text{rms}}|_{y_C}$) rather than two arbitrarily defined length scales (k_s and the location of the virtual wall), we believe that the presently discussed parametrization provides a more physical framework in which to study the problem of roughness. As suggested by Orlandi and Leonardi [19], it can provide new possibilities to model wall-bounded turbulence, arguably ranging from a boundary condition for the vertical turbulence stress in second-moment closure turbulence models to novel approaches based on the prescription of synthetic eddies on the wall; examination of these possibilities is beyond the scope of the present work and calls for extensive research in the future. We also believe that Eq. (1) can be used to assess those roughness models in which roughness is effectively accounted for without being resolved (see [45,46] for two examples of roughness models in Reynolds-averaged Navier-Stokes and DNS frameworks). These models, which are mainly based on the reproduction of the mean flow by adding source terms to the momentum equation, do not necessarily guarantee physical predictions of the turbulence statistics inside the roughness sublayer and the present parametrization can serve as a physical benchmark criterion for these classes of models.

V. CONCLUSION

Direct numerical simulation of turbulent flow in open channels with dense rough walls was carried out at $\mathrm{Re}_\tau \cong 500$ and in the fully rough regime. Fourteen different surface samples were generated using an approach based on the random distribution of roughness elements with different sizes, which allows systematic variation of surface parameters. The surface parameters independently studied in the present paper are the skewness of the surface height PDF as well as effective slope of the surface and the coefficient of variation of roughness peak heights Δ (defined as the normalized height difference between the highest and lowest roughness peaks).

The main purpose of this research was to investigate the possibility of parametrizing the roughness function using wall-normal turbulent fluctuations at the roughness crest, i.e., Eq. (1), for irregular roughness. Such a possibility was already demonstrated by Orlandi and Leonardi [18,19] for a regular roughness consisting of identical and equidistantly distributed elements. The present results suggest that for the roughness samples with similar-size elements ($\Delta = 0$) Eq. (1) makes perfect predictions. For the roughness samples with dissimilar element sizes, while this linear relation generally holds, the quality of collapse with Eq. (1) is not perfect. In this case, if the plane of crests is defined at the mean wall distance of all roughness peaks (so-called CM plane), Eq. (1) underpredicts the DNS by up to 15%. When the plane of crests is defined based on the statistical height of the highest roughness peaks (CT plane) this equation leads to a systematic overprediction of 7%–8%. Such deviations can be justified by considering the physics behind the relation of the roughness function with $v^+_{\mathrm{rms}}|_{y_C}$. The wall normal ejections caused by the roughness elements interact with the outside flow and create resistance, thus increasing the roughness function. In an irregular roughness, the roughness peaks and their resulting ejections take place at different wall-normal positions and the higher peaks are likely to cause stronger ejections. By evaluating v^+_{rms} at the CM plane, one excludes some strong ejections and hence obtains comparatively small values for $v^+_{\mathrm{rms}}|_{y_C}$. For the same reason, at the CT plane, larger values of $v^+_{\mathrm{rms}}|_{y_C}$ are measured. The present results indicate that the linear correlation between $v^+_{\mathrm{rms}}|_{y_C}$ and ΔU^+_C may hold reasonably well for irregular roughness too when the effective crest location is located between the two extreme cases of CT and CM planes examined in this paper. Whether or not one can find an *a priori* definition for such an effective crest is unclear to the present authors and calls for further investigation.

Additionally, the effect of roughness morphology on the scaling of Reynolds and dispersive stresses, particularly the peak values, within the roughness sublayer was investigated in the paper. It was demonstrated that, when normalized with bulk velocity, the peak values of all Reynolds stress components are considerably larger in the rough channels compared to the smooth channel at the same friction Reynolds number. In other words, the roughness increases the ratio of turbulent to mean kinetic energy. Normalization with bulk velocity leads to considerable variation of the peak values for different roughness morphologies. The dependence on the morphology vanishes to a high extent when inner scaling is applied; here only the normal streamwise Reynolds stress is somewhat affected by the geometry. Additionally, it was observed that all inner-scaled peak values of Reynolds stresses, except the normal streamwise component, are very close in the rough and smooth channels. Whether this finding is Reynolds-number independent calls for further investigation. Judging based on the DNS results available in the literature [23,32], such a Reynolds-number dependence, if it exists, can only be moderate. Contrary to the spanwise and wall-normal components, the normal streamwise Reynolds stress component is meaningfully suppressed by the presence of roughness, an already established characteristic of rough wall-bounded flow [23,33]. When it comes to the dispersive stresses, all the components, but the normal streamwise, are relatively small compared to the corresponding Reynolds stress irrespective of the morphology. The peak values of streamwise dispersive stress are comparable to the corresponding Reynolds stresses and show a significant dependence on the geometrical surface parameters.

The present results were also used to evaluate the extent of the roughness sublayer, the near-wall layer directly influenced by the presence of the roughness. It is understood that all first- and second-order one-point flow statistics, averaged in the time, streamwise, and spanwise directions, collapse well at a distance $2k_z$–$2.7k_z$ above the bottom plane, k_z being the statistical height of the highest roughness peaks with respect to the bottom plane. When local time-averaged Reynolds stresses were considered, however, it was observed that these stresses can show inhomogeneity in the streamwise and spanwise directions up to higher wall distances. Defining the extent of the roughness sublayer as the wall distance where this inhomogeneity vanishes, its values lie between $2.6k_z$ and $3.7k_z$ in the studied cases. Moreover, in this paper, a linear relation between the streamwise turbulence intensity u_{rms}/U and local normalized streamwise velocity $U/U_{\max}$ in the outer layer was confirmed for all rough cases. When the roughness function ΔU is added to U, the profiles of all rough cases collapse with that of a smooth channel. This universal diagnostic plot was suggested in Ref. [43]

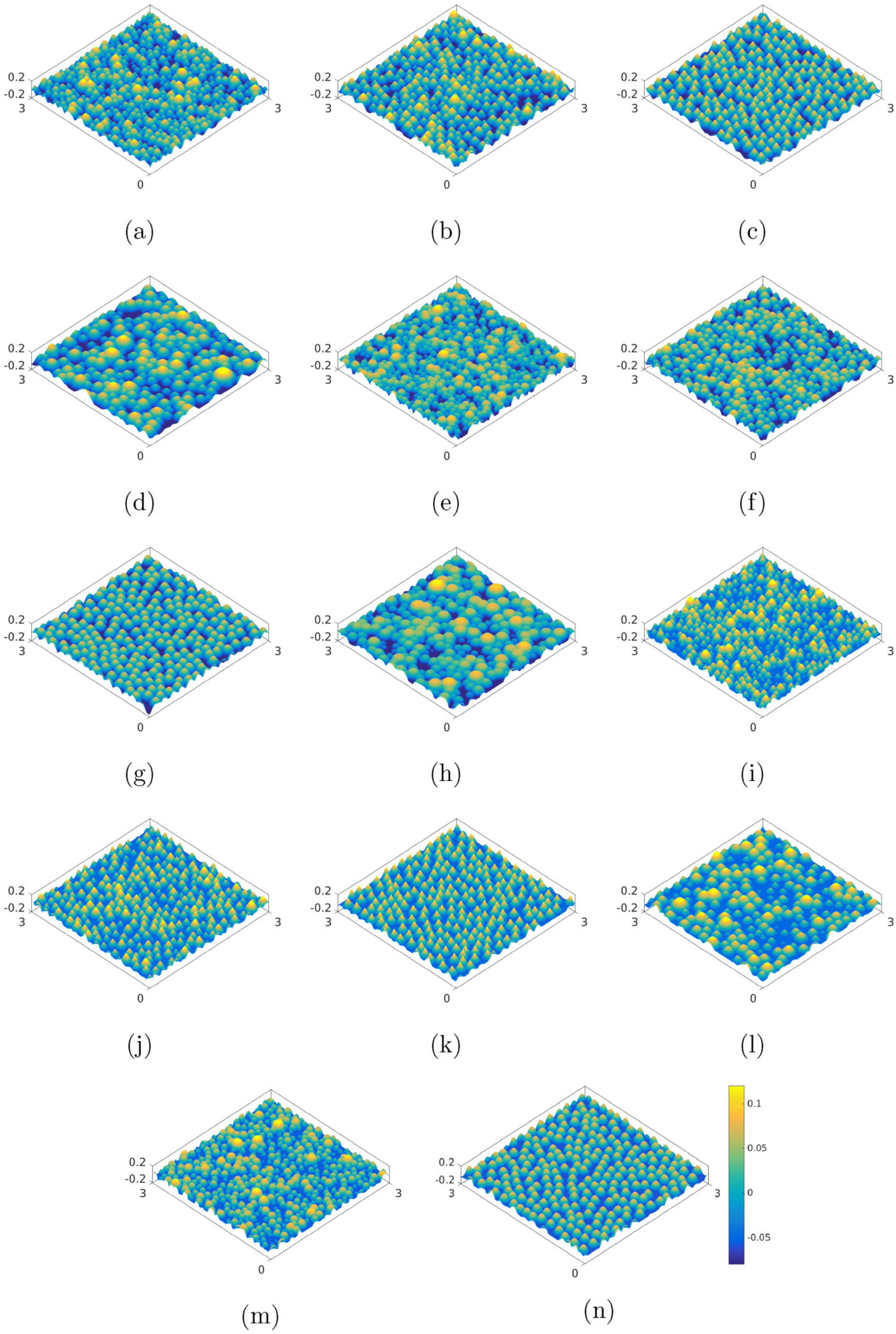

FIG. 15. The $3h \times 3h$ patches from all simulated surface samples from (a) 1 to (n) 14. Coloring indicates the surface elevation relative to the meltdown plane normalized with effective channel half-height h. All other dimensions are normalized with h.

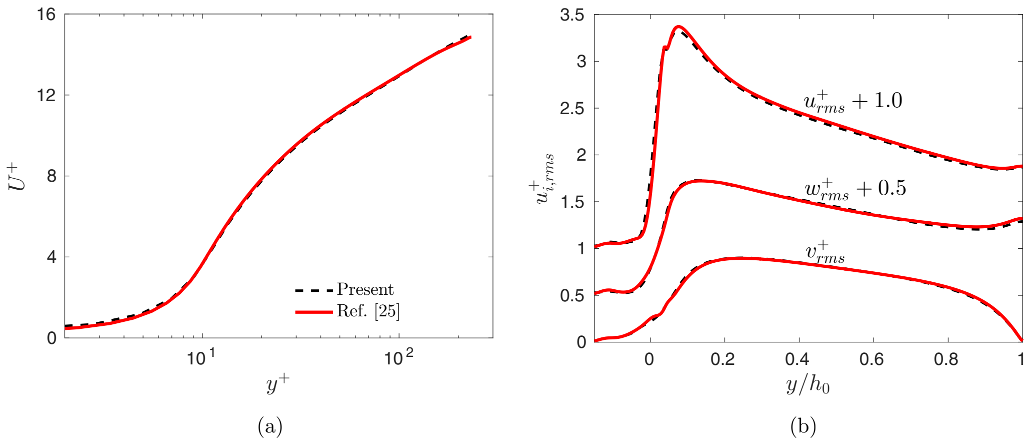

FIG. 16. Comparison of the (a) mean streamwise velocity profile and (b) rms of the diagonal turbulence stresses between the present implementation and Ref. [25].

for zero-pressure-gradient boundary layers and here its validity for the rough channels could be confirmed.

As a final comment, the simulations reported in the present paper were limited to a moderate Reynolds number ($\mathrm{Re}_\tau \approx 500$) due to the computational cost of DNS. Whether and to what extent the scaling rules discussed in this paper are valid at much higher Reynolds numbers is a question that cannot be answered with certainty using the present results. Most importantly, the correlation of the roughness function with rms wall-normal turbulent fluctuations needs to be investigated thoroughly at higher Reynolds numbers. This is a task for which a pure numerical methodology cannot be relied upon and is also difficult to fulfill experimentally as measurements at the roughness crest are complicated. How this important problem can be tackled is, in our view, a rather methodological question calling for further discussions in the future.

ACKNOWLEDGMENTS

The authors acknowledge financial support from the Deutsche Forschungsgemeinschaft under Collaborative Research Centre SFB/TRR150. The authors also thank Steffen Straub for support in the validation of the numerical implementation. The computations for this research were carried out on HPC cluster ForHLR2 at Karlsruher Institut für Technologie.

APPENDIX A

Sample patches from all surfaces outlined in Table I are displayed in Fig. 15.

TABLE III. Comparison of the numerical domain parameters between the present simulation and Ref. [25].

			Grid size	Dimensions	Grid spacings			
Work	$\mathrm{Re}_{\tau,0}$	Re_b	$N_x \times N_y \times N_z$	$L_x \times L_y \times L_z$	Δx^+	Δy^+_{min}	Δy^+_{max}	Δz^+
present	233.9	2880	$1024 \times 151 \times 256$	$12H \times H \times 3H$	3.21	0.026	2.46	3.21
Ref. [25]	235	2880	$3072 \times 256 \times 768$	$12H \times H \times 3H$	1.07	1.07	1.07	1.07

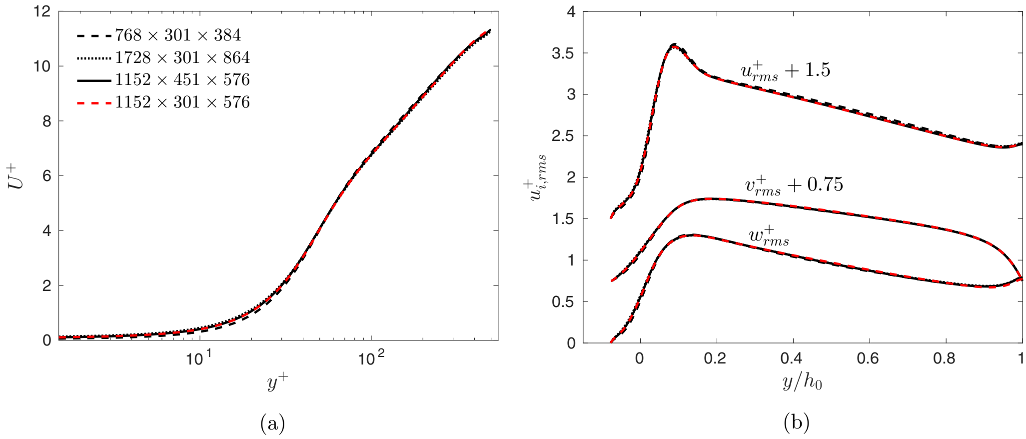

FIG. 17. Comparison of the (a) mean streamwise velocity profile and (b) rms of the diagonal turbulence stresses with various resolutions for the simulation of case 1. The domain size and Reynolds number are the same for all simulations (see Table II).

APPENDIX B

A comparison of the present implementation of the rough surface with the IBM results of case N50 in Ref. [25] with a very fine grid is provided in Fig. 16. This case consists of a roughness generated by spheres of size $H/5.6$ attached on the lower boundary of the computational domain (open channel). The present simulations are run at the same bulk Reynolds number as that of Ref. [25]. Table III summarizes the properties of the present simulations and those of Ref. [25]. It should be noted that Ref. [25] makes no distinction between Reynolds and dispersive stresses, hence here we similarly calculated the rms velocities based on the u'' components, introduced in Sec. IV, for the sake of comparison. Good agreement between the present profiles and those of Ref. [25] of first- and second-order statistics is observed in Fig. 16. In particular, the present implementation predicts the location of the Reynolds stress peaks well. Notably, the secondary peak of the streamwise component, which is in fact the dispersive stress peak, is well predicted. The largest discrepancy is in the global peak of streamwise normal stress, where the present solution shows around 2.5% underprediction. It should be mentioned that the present IBM may require higher resolutions for different geometries; for instance, we understood during the preliminary assessments of the implementation that for the prediction of flow over a square bar, a streamwise resolution of roughly twice the one shown in Table III is necessary to obtain a satisfactorily smooth solution and minimize the penetration particularly around the sharp corners.

In order to ensure the sufficiency of the resolution employed in the present simulations, a mesh-independence study for one of the cases (case 1) is done, in which the resolution is varied in both wall-parallel and wall-normal directions. Figure 17 shows the results of the mesh-independence study and it is clear that the adopted grid (dashed red line) is sufficiently fine for the first- and second-order statistics studied in the present paper.

[1] J. Jimenez, Turbulent flows over rough walls, Annu. Rev. Fluid Mech. **36**, 173 (2004).
[2] J. P. Bons, A critical assessment of Reynolds analogy for turbine flows, J. Heat Transfer **127**, 472 (2005).
[3] K. A. Flack and M. P. Schultz, Review of hydraulic roughness scales in the fully rough regime, J. Fluids Eng. **132**, 041203 (2010).
[4] A. Sigal and J. E. Danberg, New correlation of roughness density effects on the turbulent boundary layer, AIAA J. **28**, 554 (1990).

[5] J. A. van Rij, B. J. Belnap, and P. M. Ligrani Analysis and experiments on three-dimensional, irregular surface roughness, J. Fluids Eng. **124**, 671 (2002).
[6] A. A. Townsend, *The Structure of Turbulent Shear Flow*, 2nd ed. (Cambridge University Press, Cambridge, 1976).
[7] K. A. Flack, M. P. Schultz, and J. S. Connelly, Examination of a critical roughness height for outer layer similarity, Phys. Fluids **19**, 095104 (2007).
[8] K. A. Flack and M. P. Schultz, Roughness effects on wall-bounded turbulent flows, Phys. Fluids **26**, 101305 (2014).
[9] D. T. Squire, C. Morrill-Winter, N. Hutchins, M. P. Schultz, J. C. Klewicki, and I. Marusic, Comparison of turbulent boundary layers over smooth and rough surfaces up to high Reynolds numbers, J. Fluid Mech. **795**, 210 (2016).
[10] S. Leonardi, P. Orlandi, and R. A. Antonia, Properties of d- and k-type roughness in a turbulent channel flow, Phys. Fluids **19**, 125101 (2007).
[11] M. P. Schultz and K. A. Flack, Turbulent boundary layers on a systematically-varied rough wall, Phys. Fluids **21**, 015104 (2009).
[12] S. Leonardi and I. P. Castro, Channel flow over large cube roughness: A direct numerical simulation study, J. Fluid Mech. **651**, 519 (2010).
[13] M. Placidi and B. Ganapathisubramani, Effects of frontal and plan solidities on aerodynamic parameters and the roughness sublayer in turbulent boundary layers, J. Fluid Mech. **782**, 541 (2015).
[14] L. Chan, M. MacDonald, D. Chung, N. Hutchins, and A. Ooi, A systematic investigation of roughness height and wavelength in turbulent pipe flow in the transitionally rough regime, J. Fluid Mech. **771**, 743 (2015).
[15] J. Nikuradse, Strömungsgesetze in rauen Rohren, VDI-Forschungsheft Vol. 361, 1933.
[16] P. Orlandi, The importance of wall-normal Reynolds stress in turbulent rough channel flows, Phys. Fluids **25**, 110813 (2013).
[17] P. Orlandi, S. Leonardi, R. Tuzi, and R. A. Antonia, DNS of turbulent channel flow with wall velocity disturbances, Phys. Fluids **15**, 3587 (2003).
[18] P. Orlandi and S. Leonardi, DNS of turbulent channel flows with two- and three-dimensional roughness, J. Turbul. **7**, N73 (2006).
[19] P. Orlandi and S. Leonardi, Direct numerical simulation of three-dimensional turbulent rough channels: Parameterization and flow physics, J. Fluid Mech. **606**, 399 (2008).
[20] P. Orlandi, DNS of transitional rough channels, J. Turbul. **12**, N29 (2011).
[21] J. H. Lee, A. Seena, S. H. Lee, and H. J. Sung, Turbulent boundary layers over rod-and cube-roughened walls, J. Turbul. **13**, N40 (2012).
[22] E. Napoli, V. Armenio, and M. DeMarchis, The effect of the slope of irregularly distributed roughness elements on turbulent wall-bounded flows, J. Fluid Mech. **613**, 385 (2008).
[23] J. Yuan and U. Piomelli, Estimation and prediction of the roughness function on realistic surfaces, J. Turbul. **15**, 350 (2014).
[24] P. Forooghi, A. Stroh, F. Magagnato, S. Jakirlic, and B. Frohnapfel, Towards a universal roughness correlation, J. Fluids Eng. **139**, 121201 (2017).
[25] C. Chan-Braun, M. Garca-Villalba, and M. Uhlmann, Force and torque acting on particles in a transitionally rough open-channel flow, J. Fluid Mech. **684**, 441 (2011).
[26] M. Mazzuoli and M. Uhlmann, Direct numerical simulation of open-channel flow over a fully rough wall at moderate relative submergence, J. Fluid Mech. **824**, 722 (2017).
[27] K. Bhaganagar, J. Kim, and G. Coleman, Effect of roughness on wall-bounded turbulence, Flow, Turbul. Combust. **72**, 463 (2004).
[28] K. Bhaganagar, Direct numerical simulation of unsteady flow in channel with rough walls, Phys. Fluids **20**, 101508 (2008).
[29] M. Seddighi, S. He, D. Pokrajac, T. O'Donoghue, and A. E. Vardy, Turbulence in a transient channel flow with a wall of pyramid roughness, J. Fluid Mech. **781**, 226 (2015).
[30] J. Cardillo, Y. Chen, G. Araya, J. Newman, K. Jansen, and L. Castillo, DNS of a turbulent boundary layer with surface roughness, J. Fluid Mech. **729**, 603 (2013).

[31] M. Thakkar, A. Busse, and N. D. Sandham, Surface correlations of hydrodynamic drag for transitionally rough engineering surfaces, J. Turbul. **18**, 138 (2017).

[32] A. Busse, M. Lützner, and N. D. Sandham, Direct numerical simulation of turbulent flow over a rough surface based on a surface scan, Comput. Fluids **116**, 129 (2015).

[33] P. M. Ligrani and R. J. Moffat, Structure of transitionally rough and fully rough turbulent boundary layers, J. Fluid Mech. **162**, 69 (1986).

[34] L. Chau and K. Bhaganagar, Understanding turbulent flow over ripple-shaped random roughness in a channel, Phys. Fluids **24**, 115102 (2012).

[35] K. Bhaganagar and L. Chau, Characterizing turbulent flow over 3-D idealized and irregular rough surfaces at low Reynolds number, Appl. Math. Model. **39**, 6751 (2015).

[36] J. P. Bons, R. P. Taylor, S. T. McClain, and R. B. Rivir, *ASME Turbo Expo 2001: Power for Land, Sea, and Air* (ASME, New York, 2001), paper 2001-GT-0163, p. V003T01A042.

[37] M. Chevalier, P. Schlatter, A. Lundbladh, and D. S. Henningson, SIMSON, A pseudo-spectral solver for incompressible boundary layer flows, KTH Report No. TRITA-MEK 2007:7, 2007.

[38] A. Lozano-Durán and J. Jiménez, Effect of the computational domain on direct simulations of turbulent channels up to Ret = 4200, Phys. Fluids **26**, 011702 (2014).

[39] D. Goldstein, R. Handler, and L. Sirovich, Modeling a no-slip flow boundary with an external force field, J. Comput. Phys. **105**, 354 (1993).

[40] P. S. Jackson, On the displacement height in the logarithmic velocity profile, J. Fluid Mech. **111**, 15 (1981).

[41] M. R. Raupach, R. A. Antonia, and S. Rajagopalan, Rough-wall turbulent boundary layers, Appl. Mech. Rev. **44**, 1 (1991).

[42] P. H. Alfredsson, A. Segalini, and R. Örlü, A new scaling for the streamwise turbulence intensity in wall-bounded turbulent flows and what it tells us about the outer peak, Phys. Fluids **23**, 041702 (2011).

[43] P. H. Alfredsson, R. Örlü, and A. Segalini, A new formulation for the streamwise turbulence intensity distribution in wall-bounded turbulent flows, Eur. J. Mech. B **36**, 167 (2012).

[44] I. P. Castro, A. Segalini, and P. H. Alfredsson, Outer-layer turbulence intensities in smooth-and rough-wall boundary layers, J. Fluid Mech. **727**, 119 (2013).

[45] R. P. Taylor, H. W. Coleman, and B. K. Hodge, Prediction of turbulent rough-wall skin friction using a discrete element approach, J. Fluids Eng. **107**, 251 (1985).

[46] A. Busse and N. D. Sandham, Parametric forcing approach to rough-wall turbulent channel flow, J. Fluid Mech. **712**, 169 (2012).